





























## A Highly Magnified Star at Redshift 6.2

1 BRIAN WELCH <sup>1</sup>, DAN COE <sup>2,3</sup>, JOSE M. DIEGO <sup>4</sup>, ADI ZITRIN <sup>5</sup>, ERIK ZACKRISSON <sup>6</sup>,  
2 PAOLA DIMAURO <sup>7</sup>, YOLANDA JIMÉNEZ-TEJA <sup>8</sup>, PATRICK KELLY <sup>9</sup>, GUILLAUME MAHLER <sup>10,11,12</sup>,  
3 MASAMUNE OGURI <sup>13,14,15</sup>, F.X. TIMMES <sup>16,17</sup>, ROGIER WINDHORST <sup>16</sup>, MICHAEL FLORIAN <sup>18</sup>,  
4 S. E. DE MINK <sup>19,20,21</sup>, ROBERTO J. AVILA <sup>2</sup>, JAY ANDERSON<sup>2</sup>, LARRY BRADLEY <sup>2</sup>,  
5 KEREN SHARON <sup>10</sup>, ANTON VIKAEUS <sup>6</sup>, STEPHAN MCCANDLISS <sup>1</sup>, MARUŠA BRADAČ <sup>22</sup>,  
6 JANE RIGBY <sup>23</sup>, BRENDA FRYE <sup>18</sup>, SUNE TOFT <sup>24,25</sup>, VICTORIA STRAIT <sup>22</sup>,  
7 MICHELE TRENTI <sup>26,27</sup>, SONIYA SHARMA <sup>23</sup>, FELIPE ANDRADE-SANTOS <sup>28,21</sup> AND  
8 TOM BROADHURST <sup>29,30,31</sup>

9 <sup>1</sup>*Center for Astrophysical Sciences, Department of Physics and Astronomy, The Johns Hopkins University, 3400 N*  
10 *Charles St. Baltimore, MD 21218, USA*

11 <sup>2</sup>*Space Telescope Science Institute (STScI), 3700 San Martin Drive, Baltimore, MD 21218, USA*

12 <sup>3</sup>*Association of Universities for Research in Astronomy (AURA) for the European Space Agency (ESA), STScI,*  
13 *Baltimore, MD, USA*

14 <sup>4</sup>*Instituto de Física de Cantabria (CSIC-UC). Avda. Los Castros s/n. 39005 Santander, Spain*

15 <sup>5</sup>*Physics Department, Ben-Gurion University of the Negev, P.O. Box 653, Be'er-Sheva 84105, Israel*

16 <sup>6</sup>*Observational Astrophysics, Department of Physics and Astronomy, Uppsala University, Box 516, SE-751 20*  
17 *Uppsala, Sweden*

18 <sup>7</sup>*Observatório Nacional, Ministério da Ciência, Tecnologia, Inovação e Comunicações, Rua General José Cristino, 77,*  
19 *São Cristóvão, 20921-400, Rio de Janeiro, Brazil*

20 <sup>8</sup>*Instituto de Astrofísica de Andalucía, Glorieta de la Astronomía s/n, 18008 Granada, Spain*

21 <sup>9</sup>*School of Physics and Astronomy, University of Minnesota, 116 Church Street SE, Minneapolis, MN 55455, USA*

22 <sup>10</sup>*Department of Astronomy, University of Michigan, 1085 S. University Ave, Ann Arbor, MI 48109, USA*

23 <sup>11</sup>*Institute for Computational Cosmology, Durham University, South Road, Durham DH1 3LE, UK*

24 <sup>12</sup>*Centre for Extragalactic Astronomy, Durham University, South Road, Durham DH1 3LE, UK*

25 <sup>13</sup>*Research Center for the Early Universe, University of Tokyo, Tokyo, 113-0033, Japan*

26 <sup>14</sup>*Department of Physics, University of Tokyo, Tokyo 113-0033, Japan*

27 <sup>15</sup>*Kavli Institute for the Physics and Mathematics of the Universe (Kavli IPMU, WPI), University of Tokyo, Chiba*  
28 *277-8582, Japan*

<sup>16</sup>*School of Earth and Space Exploration, Arizona State University, Tempe, AZ 85287, USA*

<sup>17</sup>*Joint Institute for Nuclear Astrophysics - Center for the Evolution of the Elements, Tempe, AZ 85287, USA*

<sup>18</sup>*Department of Astronomy, Steward Observatory, University of Arizona, 933 North Cherry Avenue, Tucson, AZ 85721, USA*

<sup>19</sup>*Max-Planck-Institut für Astrophysik, Karl-Schwarzschild-Straße 1, 85741 Garching, Germany*

<sup>20</sup>*Anton Pannekoek Institute for Astronomy and GRAPPA, University of Amsterdam, NL-1090 GE Amsterdam, The Netherlands*

<sup>21</sup>*Center for Astrophysics | Harvard & Smithsonian, 60 Garden Street, Cambridge, MA 02138, USA*

<sup>22</sup>*Department of Physics, University of California, Davis, CA 95616, USA*

<sup>23</sup>*Observational Cosmology Lab, NASA Goddard Space Flight Center, Greenbelt, MD 20771, USA*

<sup>24</sup>*Cosmic Dawn Center (DAWN), Copenhagen, Denmark*

<sup>25</sup>*Niels Bohr Institute, University of Copenhagen, Jagtvej 128, Copenhagen, Denmark*

<sup>26</sup>*School of Physics, University of Melbourne, Parkville VIC 3010, Australia*

<sup>27</sup>*ARC Centre of Excellence for All-Sky Astrophysics in 3 Dimensions, University of Melbourne, Parkville VIC 3010, Australia*

<sup>28</sup>*Clay Center Observatory, Dexter Southfield, 20 Newton Street, Brookline, MA 02445, USA*

<sup>29</sup>*Department of Theoretical Physics, University of the Basque Country UPV/EHU, Bilbao, Spain*

<sup>30</sup>*Donostia International Physics Center (DIPC), 20018 Donostia, Spain*

<sup>31</sup>*IKERBASQUE, Basque Foundation for Science, Bilbao, Spain*

## ABSTRACT

Galaxy clusters magnify background objects through strong gravitational lensing. Typical magnifications for lensed galaxies are factors of a few but can also be as high as tens or hundreds, stretching galaxies into giant arcs<sup>1;2</sup>. Individual stars can attain even higher magnifications given fortuitous alignment with the lensing cluster. Recently, several individual stars at redshift  $z \sim 1 - 1.5$  have been discovered, magnified by factors of thousands, temporarily boosted by microlensing<sup>3;4;5;6</sup>. Here we report observations of a more distant and persistent magnified star at redshift  $z_{\text{phot}} = 6.2 \pm 0.1$ , 900 Myr after the Big Bang. This star is magnified by a factor of thousands by the foreground galaxy cluster lens

58 **WHL0137–08** ( $z = 0.566$ ), as estimated by four independent lens models. Unlike  
 59 previous lensed stars, the magnification and observed brightness (AB mag **27.2**)  
 60 have remained roughly constant over 3.5 years of imaging and follow-up. The  
 61 delensed absolute UV magnitude  $M_{UV} = -10 \pm 2$  is consistent with a star of  
 62 mass  $M > 50M_{\odot}$ . Confirmation and spectral classification are forthcoming from  
 63 approved observations with the *James Webb Space Telescope*.

### 64 1. A SINGLE STAR IN THE FIRST BILLION YEARS

65 The Reionization Lensing Cluster Survey (RELICS<sup>7</sup>) Hubble Space Telescope (*HST*) Treasury Pro-  
 66 gram obtained *HST* Advanced Camera for Surveys (ACS) optical imaging and Wide Field Camera  
 67 3 infrared (WFC3/IR) imaging of a total of 41 lensing clusters. Included in these observations was a  
 68 15''-long lensed arc of a galaxy at  $z_{\text{phot}} = 6.2 \pm 0.1$ <sup>8</sup>, designated WHL0137-zD1 and nicknamed the  
 69 “Sunrise Arc” (see Extended Data Table 1 and Extended Data Figure 1 for photometry and redshift  
 70 estimate details). Its length rivals the “Sunburst Arc” at  $z = 2.4$ , the brightest strongly lensed  
 71 galaxy known<sup>1;9</sup>. Within this  $z > 6$  galaxy, we have identified a highly magnified star sitting atop  
 72 the lensing critical curve at RA, Dec = 01:37:23.232, –8:27:52.20 (J2000). This object is designated  
 73 WHL0137-LS, and we nickname the star “Earendel” from the Old English word meaning “morning  
 74 star”, or “rising light”. Follow-up *HST* imaging revealed Earendel is not a transient caustic crossing  
 75 event; its high magnification has persisted for 3.5 years (see Extended Data Figure 2).

76 We can deduce qualitatively that the magnification of this object must be high given its position  
 77 within the arc. Multiple images of lensed objects appear on opposite sides of the lensing critical  
 78 curve, with the critical curve bisecting the two images. Earendel appears at the midpoint between  
 79 two images of a star cluster (1.1a/1.1b in Figure 1). We only see one image of Earendel, indicating  
 80 that its two lensed images are unresolved. Thus, the critical curve must fall near the image of the  
 81 star, indicating that it will have a high magnification.

82 Our detailed lens modeling supports this interpretation. We model the cluster using four independent  
 83 techniques: Light-Traces-Mass (LTM<sup>10;11;12</sup>), Lenstool<sup>13;14</sup>, Glafic<sup>15</sup>, and WSLAP+<sup>16;17</sup>. To constrain

84 these models, we identify two triply-lensed clumps 1.1a/b/c and 1.7a/b/c within the Sunrise Arc and  
 85 one triply-lensed clump within a  $z \sim 3$  galaxy to the north (see Extended Data Figure 3). Given  
 86 these modest constraints, our lens models retain a significant degree of freedom. Yet all our models  
 87 put Earendel within  $D_{\text{crit}} < 0.1''$  of the critical curve.

88 Each lens model includes some uncertainty on the model parameters. To understand the effect of  
 89 these uncertainties, we sampled the posterior distribution generated by the LTM lens model, and  
 90 generated critical curves from each resultant parameter set. These critical curves are shown in Figure  
 91 2. We find the star to be within  $0.1''$  in  $\sim 80\%$  of models, while the maximum distance reaches  $0.4''$ .  
 92 We then derived tighter constraints on the distance to the critical curve based on the fact that we  
 93 observe only a single unresolved object. If Earendel were farther from the critical curve, we would  
 94 see two multiple images, as with clumps 1.1a and 1.1b. The single image means either that its two  
 95 images are spatially unresolved or that microlensing is suppressing the flux of one image. We deem  
 96 the latter unlikely given that this cluster has an optically thick microlensing network at the location  
 97 of the star (see §2.6.2 for details). In this configuration, there are no pockets of low magnification  
 98 which could hide one of the images, as the microcaustics all overlap. Therefore we conclude the two  
 99 lensed images are unresolved in the current HST WFC3/IR imaging. This is consistent with our  
 100 original lens model-independent interpretation suggesting it is directly on the critical curve.

101 We then use the fact that the two images of the star are unresolved to determine the maximum  
 102 allowed distance to the critical curve. We analyze super-sampled drizzled images and find that two  
 103 lensed images would be spatially resolved if they were separated by  $0.11''$  along the arc (see Extended  
 104 Data Figure 4). Moving each image  $0.055''$  along the arc puts them  $< 0.036''$  from the critical curve,  
 105 given the angle between the arc and critical curve in the various lens models (see §2.5 for details).  
 106 Maximum distances to the critical curve ( $D_{\text{crit}}$ ) for each lens model are tabulated in Table 1. This is  
 107 a more precise determination than is possible with the weakly constrained lens models alone.

108 Using the maximum allowed separation, we can calculate the minimum magnification of the lensed  
 109 star. In the vicinity of the critical curve, magnifications are inversely proportional to the distance to

110 the critical curve:

$$\mu = \mu_0 / D_{\text{crit}} \quad (1)$$

111 where  $D_{\text{crit}}$  is expressed in arcseconds, and  $\mu_0$  is a constant that varies between lens models<sup>18</sup>. The  
 112 value of  $\mu_0$  depends on the slope of the lens potential, with flatter potentials yielding higher values of  
 113  $\mu_0$  and thus higher magnifications for a given distance (i.e. LTM), while steeper potentials give lower  
 114 magnifications (i.e. Lenstool). Due to the paucity of lensing constraints, we can only determine the  
 115 slope of the potential to within a factor of 6. However, using multiple lens models, including two  
 116 Glafic models with one flatter (lower concentration  $c = 1$ ) and one steeper ( $c = 7$ ) potential, we are  
 117 able to cover the full range of possible outcomes.

118 Based on this analysis, we derive magnification estimates summarized in Table 1. Note the magnifi-  
 119 cation calculated from Equation 1 accounts for only one of the two unresolved images. We therefore  
 120 double this value to get the total magnification from the source to the unresolved image. At the  
 121 nominal estimated distances  $D_{\text{crit}}$ , the magnification estimates range from  $2\mu \sim 1400$  (Lenstool) to  
 122  $\sim 8400$  (LTM). Given the uncertainty on  $D_{\text{crit}}$ , these values may be 0.7 – 5.0 times smaller or larger  
 123 (68% confidence). Thus the full range of likely magnifications is  $2\mu = 1000 - 40000$ . This factor of  
 124 40 uncertainty is much larger than found for lensed galaxies with typical magnifications of a few<sup>19</sup>,  
 125 due to the rapid changes in magnification that occur in the vicinity of lensing critical curves. Future  
 126 observations will significantly shrink these error bars.

127 Lower magnifications (at larger  $D_{\text{crit}}$ ) are excluded because Earendel is unresolved. Higher magnifi-  
 128 cations are allowed as the star approaches the caustic. However, based on the cluster stellar mass  
 129 density in the vicinity of the arc (Extended Data Figure 5, Extended Data Table 2, §2.6.1) we find  
 130 that the network of microlensing caustics in the star’s vicinity is optically thick (see §2.5). Given this  
 131 microlensing configuration we estimate the maximum magnification to be of order  $\mu \lesssim 10^5$ , even for a  
 132 transient caustic crossing<sup>20;21;18;22</sup>. Microlensing also has the effect of causing fluctuations in observed  
 133 brightness as the lensed star traverses the microcaustic network. However, due to the optically thick  
 134 microlensing network we find a 65% probability of the observed brightness staying within a factor of

135 2 over the 3.5 year span of our observations (Extended Data Figure 6). This is consistent with our  
 136 observed factor  $\sim 1.4$  variation (see §2.6.2 for details).

137 Our strongest evidence that Earendel is an individual star or binary rather than a star cluster comes  
 138 from our derived  $1\sigma$  upper limit on its radius. This limit ranges from  $r < 0.09$  pc to  $r < 0.36$  pc,  
 139 depending on the lens model. We derive these limits by comparing sheared Gaussian images of various  
 140 widths to the super-sampled images to determine what sizes are consistent with our observations of  
 141 a spatially unresolved object (§2.5).

142 All of the lens models yield a radius limit that is smaller than any known star cluster, indicating  
 143 that this object is more likely an individual star system. The smallest compact star clusters known  
 144 have typical radii of order  $\sim 1$  pc, with the smallest single example known having a virial radius of  
 145  $0.7$  pc<sup>23;24</sup>. Our largest radius constraint is a factor of two smaller than this star cluster, while our  
 146 tightest constraint is nearly an order of magnitude smaller. Objects at high redshift may differ from  
 147 those seen in the local universe, so we also consider observations and simulations of other high-redshift  
 148 objects. Bouwens et al.<sup>25</sup> have measured radii as small as tens of pc for very low luminosity galaxies at  
 149  $6 < z < 8$ , and Vanzella et al.<sup>26</sup> report  $r < 13$  pc star clusters in a  $z = 6.143$  galaxy that is strongly  
 150 lensed though not on the lensing critical curve. Recent simulations<sup>27</sup> resolve star-forming clumps on  
 151 scales of tens of pc in  $z \sim 2$  disks. Our constraints of  $r < 0.09 - 0.36$  pc probe significantly smaller  
 152 scales than these state-of-the-art high-redshift studies. We expect future spectroscopic observations  
 153 with JWST to conclusively determine that Earendel is one or more individual stars rather than a  
 154 star cluster.

155 Most stars of mass  $M > 15M_{\odot}$  are observed in binary systems, with a companion at a separation  
 156 of  $< 10$  AU<sup>28;29</sup>. This is well within our observational radius constraint, suggesting that Earendel is  
 157 likely composed of multiple stars. However, the mass ratio of these binaries is generally small,  $\sim 0.5$   
 158 or less<sup>30</sup>. In such systems, the light from the more massive (and thus brighter) star would dominate  
 159 our observation. For our primary analysis, we therefore assume that most of the light we observe is  
 160 coming from a single star. The binary case is discussed further in §2.7.

161 With a magnification between  $\mu = 1000 - 40000$ , we find Earendel has a delensed flux  $1 - 50$  pJy  
 162 (AB mag  $38.7 - 34.6$ ) in the F110W filter ( $0.9 - 1.4 \mu\text{m}$ ), corresponding to an absolute UV ( $1600\text{\AA}$ )  
 163 magnitude  $-8 > M_{AB} > -12$ . Based on this, we constrain Earendel’s luminosity as a function of  
 164 temperature in the H-R diagram (Figure 3), using a combination of blackbody stellar spectra at high  
 165 temperatures ( $T_{\text{eff}} > 40000$  K) and stellar atmosphere models at lower temperatures (details can be  
 166 found in §2.7).

167 We compare these constraints to stellar evolution models from Bonn Optimized Stellar Tracks  
 168 (BoOST<sup>31</sup>). We find Earendel’s derived luminosity is consistent with a single massive star with  
 169 initial mass  $\sim 40 - 500M_{\odot}$  at Zero Age Main Sequence (ZAMS). Note Figure 3 shows a fiducial low  
 170 metallicity ( $0.1Z_{\odot}$ ), as might be expected for a  $z \sim 6$  galaxy<sup>32</sup>, but we explore other metallicities  
 171 in §2.7 and Extended Data Figure 7, finding this does not significantly change our mass estimates  
 172 given the currently large uncertainties. This single star would either be a massive O-type star on  
 173 the main sequence with effective temperature  $\sim 60000$  K and mass  $> 100M_{\odot}$  or an evolved O, B, or  
 174 A-type star with mass  $> 40M_{\odot}$  and temperature anywhere from  $\sim 8000 - 60000$  K. Folding in the  
 175 times spent at Earendel’s derived luminosity for each track and the greater relative abundances of  
 176 less massive stars, we find masses between  $50 - 100 M_{\odot}$  and temperatures above  $20000\text{K}$  are most  
 177 likely (see §2.7, Extended Data Figure 8).

178 We estimate the probability of observing a star of mass  $M \gtrsim 100M_{\odot}$  in a caustic-crossing galaxy like  
 179 the Sunrise Arc to be up to a few percent, making this a fortunate yet reasonable discovery given  
 180 tens of such galaxies have been observed (see §2.8 for details).

181 The spectral type, temperature, and mass of the star remain uncertain. Future spectroscopic obser-  
 182 vations with our approved JWST program (GO 2282; PI Coe) will determine these properties for  
 183 Earendel and place it on the H-R diagram.

## REFERENCES

- 184 [1]Rivera-Thorsen, T.E. *et al.* The Sunburst Arc: Direct Lyman  $\alpha$  escape observed in the brightest known  
185 lensed galaxy. *Astron. Astrophys.* **608**, L4 (2017).
- 186 [2]Johnson, T. L. *et al.* Star Formation at  $z = 2.481$  in the Lensed Galaxy SDSS J1110+6459: Star Formation  
187 Down to 30 pm Scales. *Astrophys. J. Lett.* **843**, L21 (2017).
- 188 [3]Kelly, P. L. *et al.* Extreme magnification of an individual star at redshift 1.5 by a galaxy-cluster lens.  
189 *Nature Astronomy* **2**, 334-342 (2018).
- 190 [4]Rodney, S. A. *et al.* Two peculiar fast transients in a strongly lensed host galaxy. *Nature Astronomy* **2**,  
191 324-333 (2018).
- 192 [5]Chen, W. *et al.* Searching for Highly Magnified Stars at Cosmological Distances: Discovery of a REDshift  
193 0.94 Supergiant in Archival Images of the Galaxy Cluster MACS J0416.1-2403. *Astrophys. J.* **881**, 8  
194 (2019).
- 195 [6]Kaurov, A. A., Dai, L., Venumadhav, T., Miralda-Escudé, J. & Frye, B. Highly Magnified Stars in Lensing  
196 Clusters: New Evidence in a Galaxy Lensed by MACS J0416.1-2403. *Astrophys. J.* **881**, 58 (2019).
- 197 [7]Coe, D. *et al.* RELICS: Reionization Lensing Cluster Survey. *Astrophys. J.* **884**, 85 (2019).
- 198 [8]Salmon, B. *et al.* RELICS: The Reionization Lensing Cluster Survey and the Brightest High- $z$  Galaxies.  
199 *Astrophys. J.* **889**, 189 (2020).
- 200 [9]Rivera-Thorsen, T. E. *et al.* Gravitational lensing reveals ionizing ultraviolet photons escaping from a  
201 distant galaxy. *Science* **366**, 738-741 (2019).
- 202 [10]Zitrin, A. *et al.* Hubble Space Telescope Combined Strong and Weak Lensing Analysis of the CLASH  
203 Sample: Mass and Magnification Models and Systematic Uncertainties. *Astrophys. J.* **801**, 44 (2015).
- 204 [11]Zitrin, A. *et al.* New multiply-lensed galaxies identified in ACS/NIC3 observations of Cl0024+1654 using  
205 an improved mass model. *Mon. Not. R. Astron. Soc.* **395**, 1319-1332 (2009).
- 206 [12]Broadhurst, T. *et al.* Strong-Lensing Analysis of A1689 from Deep Advanced Camera Images. *Astrophys.*  
207 *J.* **621**, 53-88 (2005).
- 208 [13]Jullo, E., & Kneib, J. P. Multiscale cluster lens mass mapping - I. Strong lensing modelling. *Mon. Not. R.*  
209 *Astron. Soc.* **395**, 1319-1332 (2009).
- 210 [14]Jullo, E., *et al.* A Bayesian approach to strong lensing modelling of galaxy clusters. *New Journal of*  
211 *Physics* **9**, 447 (2007).
- 212 [15]Oguri, M. The Mass Distribution of SDSS J1004+4112 Revisited. *PASJ* **62**, 1017 (2010).
- 213 [16]Diego, J. M., Tegmark, M., Protopapas, P. & Sandvik, H. B. Combined reconstruction of weak and strong  
214 lensing data with WSLAP. *Mon. Mot. R. Astron. Soc.* **375**, 958-970 (2007).



- 215 [17]Diego, J. M., Protopapas, P., Sandvik, H. B. & Tegmark, M. Non-parametric inversion of strong lensing  
216 systems. *Mon. Not. R. Astron. Soc.* **360**, 477-491 (2005).
- 217 [18]Diego, J. M. The Universe at extreme magnification. *Astron. Astrophys.* **625**, A84 (2019).
- 218 [19]Meneghetti, M. *et al.* The Frontier Fields lens modelling comparison project. *Mon. Mot. R. Astron. Soc.*  
219 **472**, 3177-3216 (2017).
- 220 [20]Venumadhav, T., Dai, L. & Miralda-Escudé, J. Microlensing of Extremely Magnified Stars near Caustics  
221 of Galaxy Clusters. *Astrophys. J.* **850**, 49 (2017).
- 222 [21]Diego, J. M. *et al.* Dark Matter under the Microscope: Constraining Compact Dark Matter with Caustic  
223 Crossing Events. *Astrophys. J.* **857**, 25 (2018).
- 224 [22]Dai, L. Statistical microlensing towards magnified high-redshift star clusters. *Mon. Mot. R. Astron. Soc.*  
225 **501**, 5538-5553 (2021).
- 226 [23]Portegies Zwart, S. F., McMillan, S. L. W. & Gieles, M. Young Massive Star Clusters. *Annu. Rev. Astron.*  
227 *Astrophys.* **48**, 431-493 (2010).
- 228 [24]Figer, D. F., McLean, I. S. & Morris, M. Massive Stars in the Quintuplet Cluster. *Astrophys. J.* **514**,  
229 202-220 (1999).
- 230 [25]Bouwens, R. J. *et al.* Very low-luminosity galaxies in the early universe have observed sizes similar to  
231 single star cluster complexes. *arXiv e-prints*, arXiv:1711.02090 (2017).
- 232 [26]Vanzella, E. *et al.* Massive star cluster formation under the microscope at  $z = 6$ . *Mon. Not. R. Astron.*  
233 *Soc.* **483**, 3618-3635 (2019).
- 234 [27]Behrendt, M., Schartmann, M. & Burkert, A. The possible hierarchical scales of observed clumps in  
235 high-redshift disc galaxies. *Mon. Not. R. Astron. Soc.* **488**, 306-323 (2019).
- 236 [28]Sana, H. *et al.* Binary Interaction Dominates the Evolution of Massive Stars. *Science* **337**, 444 (2012).
- 237 [29]Sana, H. *et al.* Southern Massive Stars at high Angular Resolution: Observational Campaign and  
238 Companion Detection. *Astrophys. J. Suppl.* **215**, 15 (2014).
- 239 [30]Moe, M. & Di Stefano, R. Mind Your Ps and Qs: The Interrelation between Period (P) and Mass-ratio (Q)  
240 Distributions of Binary Stars. *Astrophys. J. Suppl.* **230**, 15 (2017).
- 241 [31]Szécsi, D., Wunsch, R., Agrawal, P. & Langer, N. ‘Bonn’ Optimized Stellar Tracks (BoOST). Simulated  
242 Populations of Massive and Very Massive Stars for Astrophysical Applications. *arXiv e-prints*,  
243 arXiv:2004.08203 (2020).
- 244 [32]Shimizu, I., Inoue, A. K., Okamoto, T. & Yoshida, N. Nebular line emission from  $z > 7$  galaxies in a  
245 cosmological simulation: rest-frame UV to optical lines. *Mon. Not. R. Astron. Soc.* **461**, 3563-3575  
246 (2016).

Lens Model	$\mu_0$	$D_{\text{crit}}$	magnification	flux	mag	$M_{UV}$	axis ratio	radius
		"	$2\mu$	nJy	AB			pc
LTM	113	0.027	$8400^{+33600}_{-2400}$	$6^{+2}_{-5}$	$37.0^{+1.7}_{-0.4}$	$-9.8^{+1.7}_{-0.4}$	1500	< 0.09
Glafic ( $c = 1$ )	69	0.020	$6800^{+27100}_{-2000}$	$7^{+3}_{-6}$	$36.8^{+1.7}_{-0.4}$	$-10.0^{+1.7}_{-0.4}$	760	< 0.14
Glafic ( $c = 7$ )	23	0.020	$2200^{+9000}_{-600}$	$22^{+9}_{-18}$	$35.6^{+1.7}_{-0.4}$	$-11.2^{+1.7}_{-0.4}$	930	< 0.21
WSLAP	28	0.036	$1500^{+6100}_{-500}$	$32^{+13}_{-26}$	$35.1^{+1.8}_{-0.3}$	$-11.7^{+1.8}_{-0.3}$	580	< 0.33
Lenstool	18	0.026	$1400^{+5500}_{-400}$	$36^{+14}_{-29}$	$35.0^{+1.8}_{-0.3}$	$-11.8^{+1.8}_{-0.3}$	560	< 0.36

**Table 1. Magnification, flux, and radius constraints across multiple lens models** Earendel results from each lens model: magnification normalization  $\mu_0$ , nominal distance  $D$  from critical curve, resulting magnification  $2\mu$  (sum of two lensed images), delensed flux in HST F110W filter ( $0.9 - 1.4 \mu\text{m}$ ), delensed F110W magnitude, absolute UV magnitude ( $1600\text{\AA}$ ), model axis ratio of lensed image, radius upper limit. 68% confidence limit uncertainties are shown for all quantities.

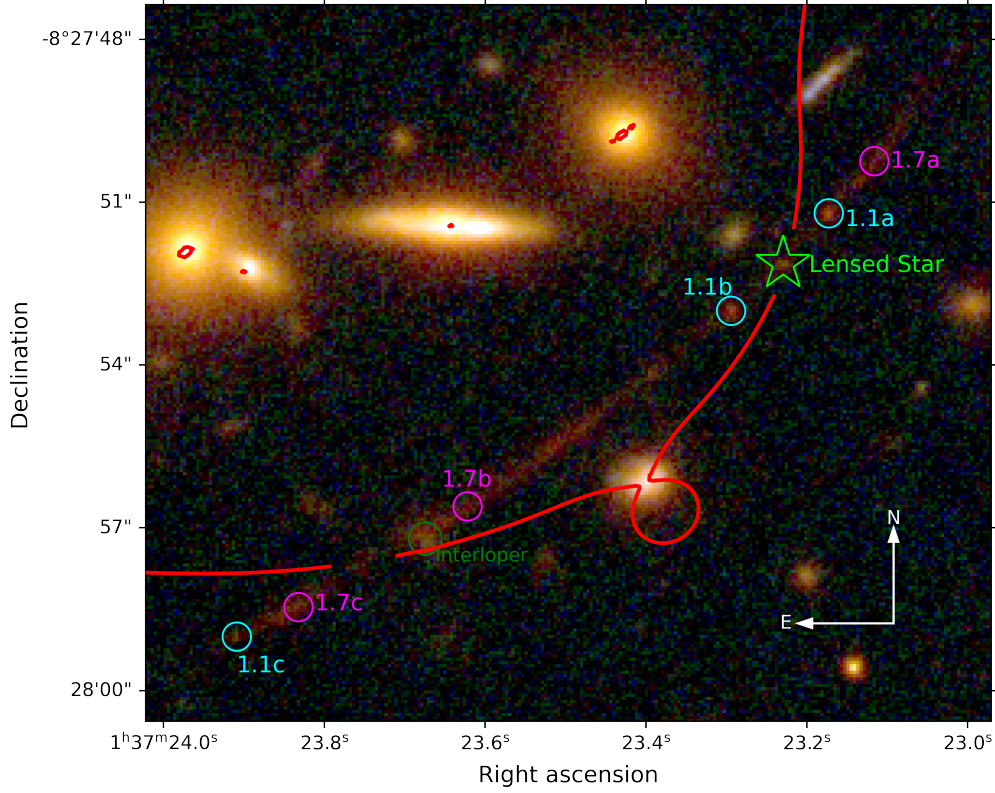


**Figure 1. Labeled color image of WHL0137-zD1** The Sunrise Arc at  $z = 6.2$  is the longest lensed arc of a galaxy at  $z > 6$ , with an angular size on the sky exceeding 15 arcseconds. The arc is triply-imaged and contains a total of seven star-forming clumps; the two systems used in lens modeling are circled, with system 1.1 in cyan and system 1.7 in magenta. The highly magnified star Earendel is labeled in green. The best-fit lensing cluster critical curve from the Light-Traces-Mass (LTM) model is shown in red, broken where it crosses the arc for clarity. The color composite image shows the F435W filter image in blue, F606W + F814W in green, and the full WFC3/IR stack (F105W + F110W + F125W + F140W + F160W) in red.

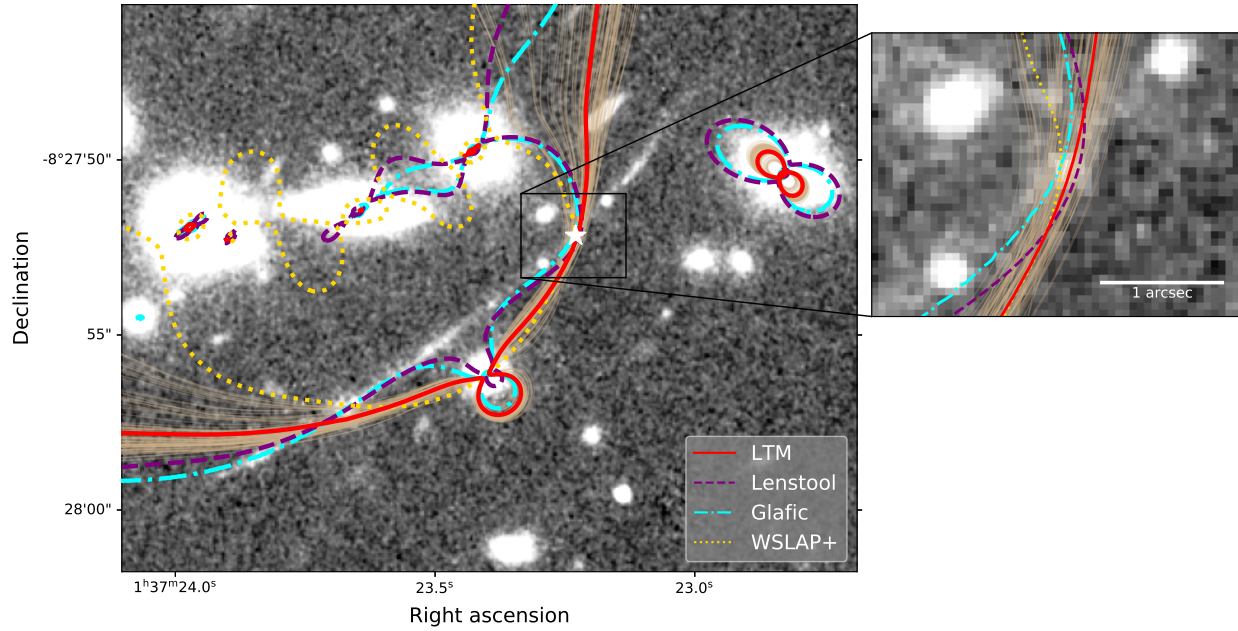


**Figure 2. Strong lensing critical curves** Our best-fit lens models all produce critical curves that cross the lensed star Earendel within  $0.1''$ . Additionally, 100 iterations of our LTM model drawn from the MCMC (thin tan lines) are similarly consistent, albeit with greater variance, all crossing the arc within  $0.4''$  of the lensed star. Critical curves are shown for LTM (red solid), Lenstool (purple dashed), Glafic (cyan dash-dot), and WSLAP+ (yellow dotted).

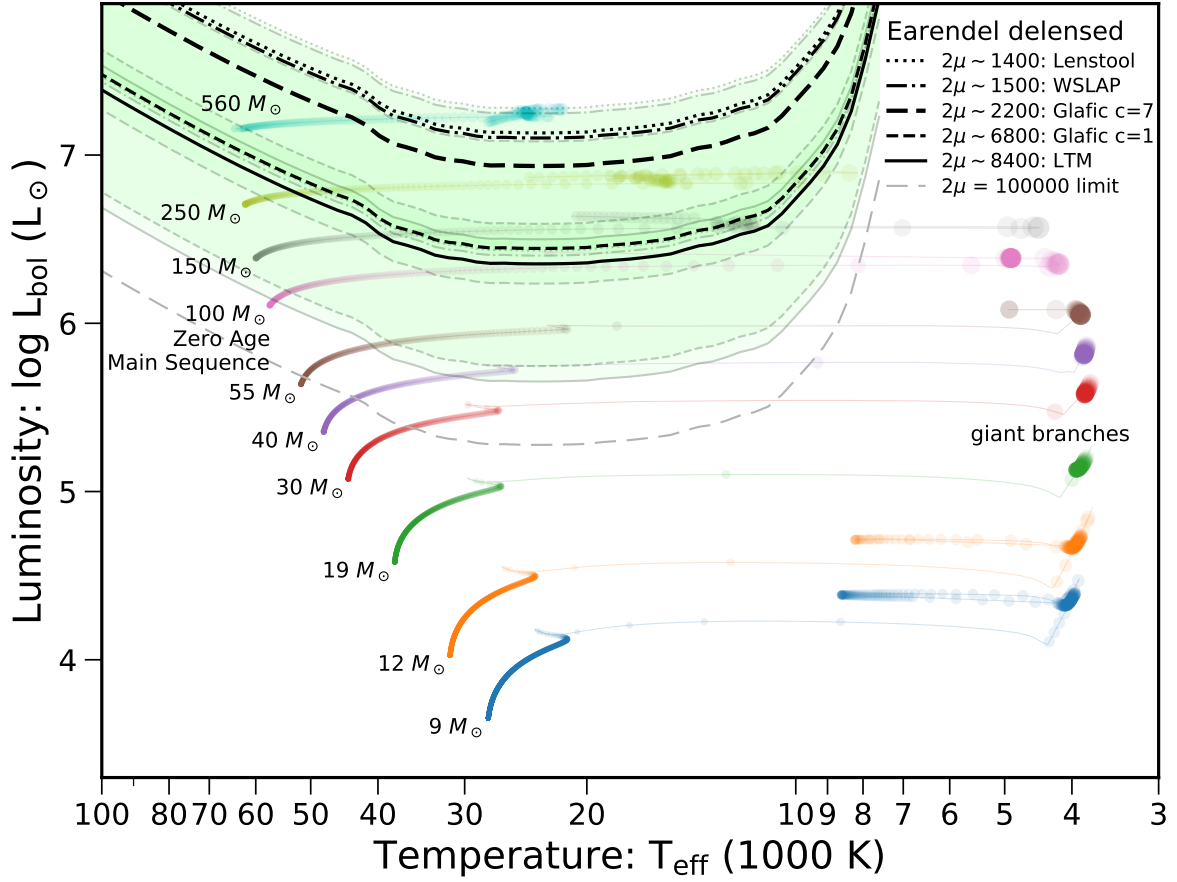


**Figure 3. Lensed star constraints on the H-R diagram** Constraints on Earendel’s luminosity and effective temperature from *HST* photometry and lensing magnification estimates, shown on an HR diagram alongside BoOST stellar evolution models (colored tracks) for stars with low metallicity ( $0.1Z_{\odot}$ )<sup>31</sup>. The green shaded region covers the 68% confidence interval of our models. All five lens models are shown, including both Glafic models with concentration  $c = 1$  and  $c = 7$ . The theoretical upper limit magnification  $\mu \sim 10^5$  is also shown; it is similar to the 95% limit for LTM. Each stellar model evolution track shows points in time steps of 10,000 years with radii scaling with stellar radius. Our luminosity constraints favor a very massive star.

## 2. METHODS

2.1. *Data*

The galaxy cluster WHL0137–08 (RA = 01:37:25, Dec = –8:27:25 [J2000]) was originally discovered as an overdensity of red luminous galaxies in SDSS images<sup>33</sup>, later confirmed at  $z = 0.566$ <sup>34</sup> based on SDSS DR12 spectroscopy<sup>35</sup>. WHL0137–08 was also ranked as the 31st most massive cluster ( $M_{500} \sim 9 \times 10^{14} M_{\odot}$ ) identified in the Planck all-sky survey PSZ2 catalog<sup>36</sup> that detected clusters via the Sunyaev-Zel’dovich (SZ) effect on the CMB, or Cosmic Microwave Background<sup>37</sup>.

WHL0137–08 was observed with *HST* as part of the RELICS Treasury program (*HST* GO 14096)<sup>7</sup>. RELICS obtained shallow imaging of 41 lensing clusters, with single-orbit depth in the ACS F435W, F606W, and F814W optical filters, and a total of two orbits divided between four WFC3/IR filters (F105W, F125W, F140W, and F160W). These observations were split over two epochs separated by 40 days for most clusters, including WHL0137–08 observed 2016-06-07 and 2016-07-17.

Salmon et al.<sup>8</sup> performed a search for high-redshift galaxies within the RELICS data, and among that sample found the 15'' long arc at  $z_{\text{phot}} = 6.2 \pm 0.1$ , here dubbed the Sunrise Arc. This impressive arc warranted followup imaging with *HST*, which was obtained 2019-11-04 and 2019-11-27 (PI Coe; *HST* GO–15842). This follow-up included an additional 5 orbits of ACS F814W imaging, along with 2 orbits each of ACS F475W and WFC3/IR F110W. These images were again split over two epochs, this time separated by 23 days. The final image was obtained 3.5 years after the first. These data were co-added to produce a full-depth image, while single epoch images were also produced to allow study of the variability of the star. Images were processed the same way as the original RELICS data<sup>7</sup>. Total exposure times and limiting magnitudes in each bandpass for our co-added images are listed in Extended Data Table 1.

We note that this cluster has also been observed with Spitzer as part of the Spitzer-RELICS program (PI Bradač). An attempt was made to extract IR fluxes from these observations<sup>38</sup>, however reliable photometry could not be obtained due to blending with brighter cluster member galaxies nearby.

2.2. *Photometry, Redshift, and SED Fitting*

273 We measured photometry using Source Extractor v2.19.5<sup>39</sup> following procedures detailed in Coe et  
 274 al.<sup>7</sup>. The Sunrise Arc was detected as 18 source segments. We summed the flux measured in all  
 275 segments, and summed the flux uncertainties in quadrature. Extended Data Table 1 provides this  
 276 total photometry for the Sunrise Arc, along with photometry for Earendel, which we identified as  
 277 one of the 18 segments.

278 We discarded the foreground interloper circled in Figure 1 from our analysis, based on its slight  
 279 positional offset, extended size, and colors consistent with a cluster member. Removing the interloper  
 280 only increases the resulting photometric redshift by 0.1.

281 We measure the Sunrise Arc’s photometric redshift using two methods: BPZ<sup>40;41</sup> and BAGPIPES<sup>42</sup>.  
 282 BPZ uses 11 spectral models (plus interpolations yielding 101 templates) spanning ranges of metal-  
 283 licities, dust extinctions, and star formation histories observed for the vast majority of real galaxies<sup>7</sup>.  
 284 BPZ also includes a Bayesian prior on the template and redshift given an observed magnitude in  
 285 F814W. We allowed redshifts up to  $z < 13$ . BPZ yields a photometric redshift of  $z_{\text{phot}} = 6.20 \pm 0.05$   
 286 (68% CL) without any significant likelihood below  $z < 5.9$  (Extended Data Figure 1).

287 BAGPIPES generates model spectra based on physical parameters, then efficiently searches a large  
 288 multidimensional parameter space to measure best-fitting parameters along with uncertainties. We  
 289 ran BAGPIPES fitting simultaneously to redshift and physical parameters as detailed in Strait et  
 290 al.<sup>38</sup>. Our choices do not significantly affect the photometric redshift, but we summarize them here.

291 We used synthetic stellar populations from BPASS v2.2.1<sup>43</sup> with nebular reprocessing and emission  
 292 lines added by the photoionization code CLOUDY<sup>44</sup>. We used a delayed star formation history that  
 293 initially rises then falls via  $SFR(t) \propto t e^{-t/\tau}$ . We use the BPASS IMF “imf135.300”: Salpeter<sup>45</sup>  
 294 slope  $\alpha = -2.35$  for  $0.5 < M/M_{\odot} < 300$ , and a shallower slope of  $\alpha = -1.3$  for lower mass stars  
 295  $0.1 < M/M_{\odot} < 0.5$ . In our BAGPIPES modeling of the Sunrise Arc, we left redshift as a free  
 296 parameter ( $z < 13$ ), along with dust (up to  $A_V = 3$  mag), stellar mass ( $10^6 - 10^{14} M_{\odot}$ ), metallicity  
 297 ( $0.005 - 5 Z_{\odot}$ ), ionization parameter ( $2 < \log(U) < 4$ ), age (from 1 Myr up to the age of the universe),  
 298 and SFR exponential decay time  $\tau$  (100 Myr – 10 Gyr). Dust extinction is implemented with the  
 299 Calzetti et al.<sup>46</sup> law, and we assume twice as much dust around all HII regions in their first 10 Myr.

300 The resulting best fit and redshift likelihood distribution are shown in Extended Data Figure 1.  
 301 BAGPIPES yields a redshift estimate  $z = 6.24 \pm 0.10$ , similar to the BPZ result without any sig-  
 302 nificant likelihood at lower redshifts. We tried explicitly exploring lower redshift  $z < 4$  solutions,  
 303 including old and/or dusty galaxies with intrinsically red spectra that can result in photometric red-  
 304 shift degeneracies for some high-redshift galaxies. But in our case, none of those red spectra can  
 305 reproduce the flat photometry observed for the Sunrise Arc in the near infrared ( $1.0 - 1.6 \mu\text{m}$ ).  
 306 BAGPIPES further yields estimates of the dust  $A_V = 0.15 \pm 0.10$  mag and mass-weighted age  $135 \pm 60$   
 307 Myr, but no strong constraints on metallicity or ionization parameter. Any estimates of stellar mass  
 308 and SFR include uncertainties due to the lensing magnification. But simply adopting a fiducial  
 309 magnification of 300 for the full arc from the LTM model, we estimate a stellar mass  $\sim 10^{7.5 \pm 0.2} M_\odot$   
 310 and current SFR  $\sim 0.3 \pm 0.1 M_\odot \text{ yr}^{-1}$ , not including magnification uncertainties.

### 311 2.3. Variability

312 Microlensing simulations suggest that the magnification, and thus observed flux, of Earendel should  
 313 remain relatively constant over time. However, some variation is expected as the star traverses the  
 314 microlensing caustic network. A factor of 1–3 difference in observed flux would be expected given  
 315 these simulations (see §2.6.2).

316 To assess the variability of the star, we study the four available epochs of *HST* imaging separately.  
 317 Images from each epoch are shown on the left in Extended Data Figure 2, where Earendel is circled  
 318 in green. Each image shows 1 orbit of WFC3/IR imaging: for RELICS, this is a WFC3/IR stack  
 319 F105W+F125W+F140W+F160W, while the follow-up imaging consists of F110W. Our analysis is  
 320 complicated by the fact that RELICS and the follow-up imaging did not use the same WFC3/IR  
 321 filters. We measure  $49 \pm 4$  nJy in the F110W imaging (sum of epochs 3 and 4) and derive a single  
 322 value  $35 \pm 9$  nJy in RELICS (epochs 1 and 2) from a weighted average of the fluxes measured in  
 323 the four WFC3/IR filters. The results are shown as horizontal bands in Extended Data Figure 2,  
 324 along with the fluxes measured in each filter individually. Note summing only the RELICS filters  
 325 F105W+F125W (closest to F110W) yields  $34 \pm 15$  nJy, similar to the result from the full stack with  
 326 larger uncertainty.



We find that the IR flux may have varied by a factor of  $\sim 1.4$  across the epochs. However, the large uncertainties on our measured flux values mean that this number is consistent with no variation. Thus we conclude that we see no significant variation across our observations. This low level of variation is consistent with our microlensing simulation results. Future observations with *HST* and *JWST* will further explore the variability of this highly magnified object.

#### 2.4. Lens Modeling

The Sunrise Arc is a highly magnified system, and the lensed star Earendel was identified by the large magnification given by our best fit lens models. Strong lensing magnifications have steep gradients in the vicinity of lensing critical curves, so to evaluate the validity of our interpretation of the arc and lensed star we have taken great care in modeling the lensing cluster. We have constructed a total of five lens models using four independent modeling programs, LTM<sup>11;10;12</sup>, Lenstool<sup>14;13</sup>, Glafic<sup>15</sup>, and WSLAP+<sup>17;16</sup>.

We utilized a total of three sets of multiple images in our lens model optimization. The multiple image systems are highlighted in Extended Data Figure 3, with each arc shown in detail within that figure. System 1 is the Sunrise Arc at  $z_{\text{phot}} = 6.2$ , and system 2 consists of three images of a bright blue knot at  $z_{\text{phot}} = 3.1$ . Within the Sunrise Arc, we use two sets of multiple images, labeled 1.1 and 1.7. Positions of multiple images 1.1 and 1.7 are defined using the F110W data, as this filter has the strongest detections for each component of the arc (SNR ranges from 7 for the faintest feature to over 20 for the brightest). 1.1 is a compact star-forming clump within the galaxy. Two of the images of 1.1 bracket the star, and are themselves highly magnified. The third image appears much fainter at the southeastern end of the arc. The apparent difference in surface brightness between these clumps is due to the fact that all three are unresolved. This fainter third image was not included in the Glafic models, while it was included in the LTM, Lenstool, and WSLAP+ models. Comparisons with LTM and Lenstool models made without including this third image show insignificant deviation from models including the third image, indicating that it may not be critical to include when our other constraints are used. The images of 1.7 consist of a clump near the opposite end of the arc. This clump is closer to the center of the host galaxy, and so it is harder to pick out among the flux of the

354 host galaxy. However, our lens models support its positioning, and it allows us to include the full  
 355 length of the arc in the lens model optimization by including a positional constraint at each end. No  
 356 additional counter-images of the arc are predicted by our lens models.

357 Cluster member galaxies were selected via the cluster red sequence<sup>47;48</sup>. We selected galaxies along  
 358 the cluster red sequence in two colors, (F435W – F606W) and (F606W – F814W). We also included  
 359 a redshift selection, only including galaxies in the range  $0.35 \leq z_{\text{phot}} \leq 0.8$ , bracketing the cluster  
 360 redshift of  $z_{\text{cluster}} = 0.566$ . After selecting galaxies that fit these criteria, we performed a visual  
 361 inspection to confirm or remove cluster members based on morphology. Finally, we chose to include  
 362 two small galaxies near the Sunrise Arc which are more questionable cluster members. These small  
 363 galaxies, marked as C and D in Extended Data Figure 3, may be small cluster members or background  
 364 galaxies, and would normally have been too faint to include in our lens models. They are only  
 365 included here due to their proximity to the arc, and thus their increased potential to impact the  
 366 lens magnification in this region. Their questionable status as cluster members led us to leave them  
 367 to be freely optimized in the LTM and `Lenstool` models, while galaxy C was excluded from the  
 368 WSLAP+ model. This galaxy is given low mass in other models (downweighted relative to its  
 369 observed magnitude), so its exclusion from the WSLAP+ model causes only minor changes in the  
 370 shape of the critical curve.

#### 371 2.4.1. *Light-Traces-Mass Lens Model*

372 The primary lens model used for this analysis was created using the Light-Traces-Mass (LTM)  
 373 method<sup>11;10;12</sup>. As the name suggests, the LTM method assumes that light approximately traces  
 374 mass within the lensing cluster. Each cluster member is assigned a power-law mass density dis-  
 375 tribution, with the overall scaling proportional to the measured flux of the galaxy. The sum of  
 376 these galaxy-scale masses is then smoothed with a Gaussian kernel of variable width to represent  
 377 the cluster-scale dark matter distribution. This simple description of the lens allows a rudimentary  
 378 lens model to be created without multiple image constraints set, as mass is assigned based on cluster  
 379 member positions and fluxes. Multiple image candidates can then be checked against the initial lens  
 380 models, which in turn are iteratively refined.

381 In this case, we began with the a priori assumption that the Sunrise Arc consisted of two images  
 382 of a single source galaxy, reflected once across the critical curve. However, initial models disfavored  
 383 this interpretation, and some exploration revealed that a triply imaged galaxy was the only way to  
 384 reproduce the full length of the arc. The other multiply imaged system at  $z \sim 3$  was initially assumed  
 385 to be triply imaged, with three clear knots showing similar photometry and morphology. These knots  
 386 were confirmed by the exploratory LTM models.

387 After the initial explorations solidified our interpretation of the multiple image constraints, we op-  
 388 timized the model using the standard LTM minimization algorithm. Briefly, the distances between  
 389 true multiple image locations and model-predicted positions are minimized using a  $\chi^2$  function.  
 390 The minimization is done with a Monte-Carlo Markov Chain (MCMC) using a Metropolis-Hastings  
 391 algorithm<sup>49</sup>.

392 During optimization, we allowed the relative weights of six galaxies (circled in Extended Data Figure  
 393 3) to be freely optimized. This allows the model additional freedom where needed. Each free galaxy  
 394 is allowed to vary individually in brightness (and thus mass) by a factor ranging from 0.5 to 3 with  
 395 a flat prior. The brightest cluster galaxy (BCG) is left free as standard. Beyond that, we allow  
 396 the two bright cluster members near system 1 (labeled A and B in Extended Data Figure 3) to  
 397 vary due to their proximity to our multiple image constraint. Similarly, the relative weights of the  
 398 galaxies labeled C and D were left free due to their proximity to the Sunrise Arc. Additionally,  
 399 the membership status of these galaxies is uncertain, as described above. Allowing their weights to  
 400 vary effectively covers the range of possibilities, from these being true cluster members to unrelated  
 401 background galaxies. Finally, galaxy E appears to be a spiral disk galaxy viewed edge-on. Such  
 402 galaxies follow a different mass-to-light ratio than elliptical galaxies, so allowing it to vary accounts  
 403 for this difference. Relative galaxy weights in the best fit model range from 0.8 to 2.2.

404 In addition to the multiple image constraints described above, we added flux constraints from the  
 405 bright knots bracketing the star, and added parity constraints to all image systems. The flux con-  
 406 straint helps to pinpoint the location of the critical curve crossing, which is of critical importance to  
 407 our analysis of this object. The parity constraints serve to counteract the proximity of our multiple

408 images. Since our images are separated by as little as  $1''$ , the MCMC optimization often found so-  
 409 lutions with a single image appearing near the midpoint of the arc. While this does provide a low  
 410  $\chi^2$ , it is clear that the released images do not look anything like the true arc. The parity constraint  
 411 requires that the critical curves pass between multiple images, giving them opposite parity. If this  
 412 constraint is not met, a penalty is added to the  $\chi^2$  function, allowing the model to avoid these local  
 413 minima and find the true solution.

414 The LTM model provides the most accurate reconstruction of the full length of the Sunrise Arc, thus  
 415 it is the one we take as our overall best fit model.

#### 416 2.4.2. *Lenstool Lens Model*

417 The accuracy of the cluster lens model is of critical importance to our analysis of this object. There-  
 418 fore, in order to confirm that our lensing interpretation is correct, we modeled the cluster lens using  
 419 additional independent software packages. The secondary package used in this analysis was the  
 420 Lenstool lens modeling software<sup>14;13</sup>.

421 Lenstool is a parametric model that utilizes a MCMC method to sample the model parameter space.  
 422 The model assigns pseudo-isothermal elliptical mass distributions (PIEMD)<sup>50</sup> to both the cluster-  
 423 scale dark matter halo as well as to individual cluster member galaxies. The total mass distribution  
 424 is a superposition of the cluster-scale mass distribution and the smaller galaxy-scale masses. Each  
 425 PIEMD model has seven free parameters: the position  $(x, y)$ , ellipticity, position angle, core radius  
 426  $r_{core}$ , truncation radius  $r_{cut}$ , and the effective velocity dispersion  $\sigma_0$ . Note  $\sigma_0$  is not precisely the  
 427 observed velocity dispersion; see Eliasdóttir et al.<sup>51</sup> for details.

428 Six of the seven parameters of the PIEMD model are left free to be optimized, with the exception  
 429 being the cut radius as this is not well constrained by strong lensing data alone. To keep the  
 430 total number of parameters from getting too large, the parameters for the galaxy-scale masses are  
 431 determined by their photometric properties, assuming a constant mass-to-light ratio. This is done  
 432 using scaling relations for the velocity dispersion  $\sigma_0 \propto L^{1/4}$  and truncation radius  $r_{cut} \propto L^{1/2}$ . The  
 433 constants of proportionality are optimized freely, while the positions, ellipticities, and position angles  
 434 are all fixed to what is measured photometrically using Source Extractor<sup>39</sup>.

435 In our modeling, we choose to leave several key galaxies free to have their velocity dispersions and  
 436 radii freely optimized. These free galaxies are highlighted in Extended Data Figure 3. As mentioned  
 437 above, the spiral galaxy (E) does not follow the same M/L relation as cluster elliptical galaxies, and  
 438 is therefore left free. We again leave the two small, white galaxies near the arc (C, D) free both  
 439 because of their proximity to the arc, and because of their questionable status as cluster members. If  
 440 these are not part of the cluster, their effect on the lensing of the arc will be much less, so we account  
 441 for that by allowing their masses to vary. Finally, two galaxies are left free near the  $z \sim 3$  system  
 442 (A, B). Each free parameter is assigned a Gaussian prior centered on the parameter value given by  
 443 the above scaling relations. The velocity dispersion priors are given a width of 15 km/s, and priors  
 444 on radius are given a width of 5 kpc. Best fit values all fall within  $\sim 2.5\sigma$  of the original value.

#### 445 2.4.3. *Glafic Lens Model*

446 The Glafic model used here was made using the publicly available Glafic lens modeling code<sup>15</sup>. Glafic  
 447 adopts a parametric lens modeling approach in which the lensing mass is built of multiple components,  
 448 each defined by a small number of parameters (position, mass, ellipticity, and position angle). Cluster  
 449 member galaxies are modeled with PIEMD mass models, while the larger cluster-scale potential is  
 450 modeled with two NFW halos<sup>52</sup> placed at the positions of the brightest and second brightest cluster  
 451 member galaxies. To reduce the total number of parameters in this model, the member galaxies are  
 452 assumed to scale with luminosity, such that the velocity dispersion  $\sigma \propto L^{1/4}$ , and the truncation  
 453 radius  $r_{cut} \propto L^\eta$  with  $\eta$  being fixed to 1 for simplicity. The normalizations of these scaling relations  
 454 are left as free parameters. The ellipticities and position angles of the member galaxies are fixed to  
 455 values measured from the images using Source-Extractor<sup>39</sup>. The parameters of the lens model are  
 456 optimized using a MCMC.

#### 457 2.4.4. *WSLAP+ Lens Model*

458 The final lens modeling package used in our analysis is the hybrid parametric/non-parametric  
 459 WSLAP+ code<sup>17;16</sup>. This modeling program divides the cluster mass distribution into a compact  
 460 component associated with cluster member galaxies, and a diffuse component representative of the

461 cluster dark matter halo. The compact component assigns mass to cluster galaxies based on their lu-  
 462 minosity via a mass-to-light ( $M/L$ ) scaling ratio. This scaling is fit to a single value for the ensemble  
 463 of cluster members during the optimization process.

464 The diffuse mass component is defined as the superposition of Gaussians on a grid. These grid cells  
 465 map the mass at any given point in the cluster, and are optimized in conjunction with the compact  
 466 galaxy masses. This non-parametric aspect of WSLAP+ gives it more freedom to assign mass where  
 467 a parametric model (such as LTM or Lenstool) might not.

468 Such non-parametric models probe a broader range of solutions, often allowing larger uncertainties for  
 469 measured quantities<sup>19</sup>. However, the increased freedom of this type of lens model can more readily fit  
 470 atypical mass distributions, meaning it is more likely to span the true solution, particularly when the  
 471 underlying mass distribution deviates from our typical mass-to-light assumptions. In this case, the  
 472 increased freedom can determine if such an atypical mass distribution could explain our observations  
 473 as a moderately magnified cluster of stars rather than a single star.

474 Instead, we find that the WSLAP+ model agrees with our parametric models, with the  $z = 6.2$   
 475 critical curve crossing within  $0.1''$  of Earendel in all models. This supports our interpretation of  
 476 Earendel as an extremely magnified single star.

### 477 2.5. Magnification and Size Constraints

478 Using the various lens models, we constrain Earendel's magnification and delensed properties as  
 479 summarized in the main text. Based on observing a single unresolved image, we place upper limits  
 480 on Earendel's radius and distance from the critical curve as illustrated in Extended Data Figure 4.

481 First, we model the source as a Gaussian light profile with a width  $\sigma$  that we refer to as the radius  $r$   
 482 (e.g., 0.1 pc). Then we stretch this Gaussian along the arc for a given model magnification  $\mu = \mu_{\parallel}\mu_{\perp}$   
 483 and axis ratio  $\mu_{\parallel}/\mu_{\perp}$  where the tangential magnification  $\mu_{\parallel} = 1/(1 - \kappa - \gamma)$  and perpendicular  
 484 magnification  $\mu_{\perp} = 1/(1 - \kappa + \gamma)$  for a lens model mass  $\kappa$  and shear  $\gamma$  at a given position (note this is  
 485 normally referred to as radial magnification as defined with respect to the BCG. However that would  
 486 be confusing in this context where Earendel's radius is magnified most significantly by the tangential  
 487 magnification  $\mu_{\parallel} \sim 1000$ , and much less so by the perpendicular or radial magnification  $\mu_{\perp} \sim 1.1 -$

488 2.1). In practice, for each model we measure  $\mu_{\perp}$  near Earendel (it varies slowly) and  $\mu_0$  from fitting  
 489  $\mu = \mu_0/D''$ . Then the observed lensed radius along the arc would be  $R = \mu_{\parallel}r = \mu_0r/D''\mu_{\perp}$ .  
 490 We convert the magnified radius to image pixels via  $1'' = 5.6$  kpc (at  $z = 6.2$ ). Note the resulting  
 491 lensed image is approximately a 1D Gaussian line (stretched almost entirely tangentially along the  
 492 arc) convolved with the HST WFC3/IR F110W PSF (point spread function).

493 Then by analyzing the HST images, we determine that a 1D Gaussian with a width of  $\gtrsim 0.055''$   
 494 would begin to appear spatially resolved. This width is roughly 0.4 native WFC3/IR pixels (each  
 495  $0.13''$ ), or  $\sim 1$  drizzled pixel ( $0.06''$ ) in our standard data products. We perform this analysis on a  
 496  $10\times$  super-sampled image (drizzled to  $0.013''$  / pixel) combining the 8 F110W exposures. Given a  
 497 model of the HST F110W PSF, we first confirm that the image of Earendel is unresolved: consistent  
 498 with and not measurably wider than the PSF. Then we stretch the PSF diagonally along the arc,  
 499 finding that it appears unresolved when convolved with a 1D Gaussian with  $\sigma = 0.055''$ . Combining  
 500 this upper limit on  $R$  with the lens model estimates of  $\mu_0$  and  $\mu_{\perp}$ , and upper limits on  $D''$  derived  
 501 below, we determine that Earendel's intrinsic delensed radius is  $r < 0.09 - 0.36$  pc, depending on the  
 502 lens model.

503 Additionally, the radius upper limit assumes that a hypothetical star cluster would sit centered on  
 504 the lensing caustic. This configuration would imply that our unresolved object is a merged pair of  
 505 images, each showing the same half of the source cluster. This specific geometry would require precise  
 506 alignment of the star cluster with the lens, making it less likely. A more likely geometry would be a  
 507 hypothetical star cluster appearing entirely on the visible side of the caustic, now creating a merging  
 508 pair of images of the full cluster. This setup would decrease our radius limits by a factor of two (to  
 509  $r < 0.045$  pc for LTM through  $r < 0.18$  pc for Lenstool), further straining the possibility that this  
 510 is a star cluster. There is a possibility that we are seeing a small fraction of a larger star cluster,  
 511 and that the rest of the cluster is hidden behind the caustic. This is also somewhat unlikely, but we  
 512 cannot rule it out.

513 Given this radius smaller than known star clusters, we determine Earendel is more likely an individual  
 514 star or star system. Such systems are significantly smaller and would certainly appear as unresolved.  
 515 Thus going forward, we assume Earendel’s light can be modeled as a point source.

516 Next we model Earendel as two lensed point sources separated by a distance  $2\xi$ . By analyzing the  
 517 HST images, we find a similar result: the two images (convolved with the PSF) can be spatially  
 518 resolved when separated by a distance  $2\xi \sim 0.11''$ , with  $\xi \sim 0.055''$ . These lensed images would  
 519 appear separated along the arc. The lensing critical curve intersects the arc at an angle  $\theta$  that varies  
 520 between  $22^\circ$  and  $41^\circ$ , depending on the lens model. The distance from each lensed image to the  
 521 critical curve is  $D = \xi \sin \theta$ . Thus, the maximum distance to the critical curve is  $D < 0.055'' \sin \theta$ ,  
 522 which varies from  $D < 0.02''$  to  $D < 0.036''$ , depending on the lens model.

523 Given  $D$ , we determine the magnification estimate  $\mu$  from each model and constraints on radius  $r$   
 524 described above, all summarized in Table 1. We note that given the strong lens model constraints  
 525 (observed multiple image locations), the critical curve can be at any small distance  $D < 0.1''$  from  
 526 Earendel with roughly equal likelihood. This translates to a magnification likelihood  $P(\mu) \propto 1/\mu$ .  
 527 We confirm this likelihood distribution in the LTM MCMC posterior range of models. We note  
 528 microlensing introduces additional scatter and uncertainty, but this is subdominant.

529 Our upper limits on  $D$  (68% confidence) translate to lower limits on  $\mu$ , given  $\mu \propto 1/D$ . Here rather  
 530 than upper limits  $D < D_1$ , we are more interested in the 68% central confidence range, which is  
 531  $0.2D_1 < D < 1.4D_1$  assuming a Gaussian likelihood. Given  $\mu \propto 1/D$  and lower limits  $\mu > \mu_1$ ,  
 532 the corresponding central confidence range is  $0.7\mu_1 < \mu < 5.0\mu_1$ . For example, at 68% confidence  
 533 LTM yields either  $2\mu > 8400$ , or  $6000 < 2\mu < 42000$ . This statistical uncertainty (a factor of 7) is  
 534 comparable to the large systematic uncertainty spanned by the various lens models (a factor of 6).  
 535 LTM yields the highest magnification estimates, while Lenstool yields the lowest:  $1000 < 2\mu < 6900$   
 536 (see Table 1). Thus, rounding slightly, we quote the full uncertainty range as  $1000 < 2\mu < 40000$  for  
 537 Earendel’s magnification.

538 We note we also attempted to measure constraints on radius and separation using a forward modeling  
 539 technique as in Johnson et al.<sup>53</sup>. However, this method is limited to the few allowed lens models that



540 each put Earendel at a discrete distance  $D$  from the critical curve. In order to determine limits on  
 541  $D$ ,  $r$ , and  $\mu$ , we needed to vary  $D$  and  $R$  smoothly. Forward model results for each model fell within  
 542 the allowed ranges derived above.

### 543 2.6. *Microlensing Effects*

544 Previous lensed star discoveries were identified when the magnification, and thus observed brightness,  
 545 temporarily increased<sup>3;4;5;6</sup>. These transients have relied on microlensing, wherein stars bound to the  
 546 lensing cluster temporarily align with the lensed image(s) of the star, creating a brief boost to  
 547 the magnification. The relative transverse motions of lensing stars with respect to the lensed star  
 548 impact the microlensing alignment and lead to the fluctuations observed in previous lensed stars.  
 549 It is possible to decrease the amplitude of these microlensing fluctuations if the optical depth of  
 550 microlenses increases. In situations where the magnification is extreme, microcaustics overlap in the  
 551 source plane resulting in relatively small fluctuations in the flux every time a microcaustic crossing  
 552 happens. The more microcaustics overlap, the less effect they have on the observed flux. This “more  
 553 is less” microlensing effect is observed when the effective optical depth of microlensing is greater  
 554 than 1 (that is, microcaustics are overlapping each other<sup>22</sup>). In this situation, the observed flux is the  
 555 sum of the fluxes from all microimages. Since the number of microimages scales with the number of  
 556 overlapping microcaustics, crossing one microcaustic results in a smaller relative change in the total  
 557 flux for a larger number of overlapping microcaustics<sup>68</sup>.

#### 558 2.6.1. *Diffuse Light Calculation*

559 Our microlensing simulations depend on the number density of stars in the line of sight to Earendel.  
 560 These can be a combination of stars or stellar remnants in the wings of cluster member galaxies,  
 561 and stars or stellar remnants not bound to any galaxy that make up the ICL. To facilitate our  
 562 microlensing analysis, we measured the cluster stellar mass density in the region around the Sunrise  
 563 Arc, combining both the ICL and faint wings of cluster galaxies. From the stellar mass density, we  
 564 can then calculate the number density of stars using an assumed initial mass function.

The full cluster light and ICL modeling analysis of WHL0137–08 is performed by Jiménez-Teja et al.<sup>69</sup>. Here we mostly care about the stellar mass density in the region around the arc, and more specifically around the lensed star. Thus we focus our measurement on two rectangular regions parallel to the arc, one on each side, extending between the two images of the brightest knot, as shown in Extended Data Figure 5. The arc, knots, and star are all masked from the image prior to measurement, but cluster member galaxies are kept as we are interested in the wings of these galaxies as well as the ICL contribution to stellar density in this region. The extent of the arc is defined in the F110W band, as that is the band in which the arc appears brightest.

The fluxes within these apertures are used to fit a stellar energy distribution (SED). The SED fitting is done using the Fitting and Assessment of Synthetic Templates (FAST) code<sup>70</sup>. We used stellar population models from Bruzual & Charlot<sup>71</sup>, along with initial mass functions from both Chabrier<sup>63</sup> and Salpeter<sup>45</sup> to explore the full range of possible solutions. With this technique, we find a stellar surface mass density of  $\Sigma_* \sim 10 M_\odot \text{pc}^{-2}$ , however the uncertainties allow for values as low as  $\sim 1 M_\odot \text{pc}^{-2}$  (see Extended Data Table 2). Since low stellar surface mass densities introduce more variability in the flux, we explore two regimes with  $\Sigma_* \sim 1 M_\odot \text{pc}^{-2}$  and  $\Sigma_* \sim 10 M_\odot \text{pc}^{-2}$ . Outside this regime, smaller values of  $\Sigma_*$  are unlikely given the observational constraints, and larger values of  $\Sigma_*$  would result in even smaller fluctuations (over time) in the observed flux.

### 2.6.2. Microlensing Simulations

To cover the range of possible diffuse light stellar surface mass densities in our microlensing analysis, we ran two simulations of the effects of microlensing on our observed magnification. One simulation assumed a value of  $\Sigma_* = 10 M_\odot \text{pc}^{-2}$ , while the other assumed a value of  $\Sigma_* = 1 M_\odot \text{pc}^{-2}$ . With these two values, we can explore both the high end density estimate, which would produce a denser microlensing caustic network and thus increase the probability that the star would appear at extreme magnification, and the low end estimate which would produce greater variability in the magnification, and a non-negligible probability that one of the two counter-images is unobserved.

Our simulations follow Diego et al.<sup>21;18</sup> Since we are assuming the two counter-images form a single unresolved image, in order to compute the total flux, we perform two simulations, one with negative

592 parity and one with positive parity. In both cases, the magnification (in absolute value  $|\mu|$ ) is the  
 593 same and equal to half the total magnification of the pair of counter-images of the star ( $2\mu$ ). We  
 594 force the two magnifications to be the same (but opposite sign) by changing slightly the values of  
 595  $\kappa$  and/or  $\gamma$ . The total flux at a given moment is given by the superposition of two tracks, one for  
 596 the simulation with positive parity and one for the simulation with negative parity. Both tracks  
 597 are forced to have the same orientation with respect to the cluster caustic. The very small scale  
 598 fluctuations observed in the tracks are due to shot noise in the ray-tracing process.

599 In the simulation, microlenses are assumed to be point-like, with masses drawn from the mass func-  
 600 tions of Spera et al.<sup>72</sup> The mass function is normalized to match our stellar surface mass density  
 601 measurements around the star. These microlenses are then distributed randomly across a circular  
 602 region of radius 10 mas, in a lens plane that has a resolution of 20 mas per pixel. For the smooth  
 603 component, or macromodel, we impose the constraint that the total convergence and shear from the  
 604 macromodel and the stellar component is consistent with our lens models. The convergence from  
 605 the smooth component is such that the total magnification is  $2\mu \approx 9000$ , when the flux from both  
 606 counter-images is combined into a single unresolved source. In particular, the convergence in the  
 607 smooth model is determined after fixing the total magnification of each counter-image as  $\mu = \mu_{\parallel}\mu_{\perp}$ ,  
 608 where  $\mu_{\parallel}$  and  $\mu_{\perp}$  are the tangential and perpendicular magnifications, respectively. This results in a  
 609 total average magnification (when integrating over long periods of time) of  $2\mu = 8960$ , close to the  
 610 desired fiducial value  $2\mu = 9000$ .

611 The magnification in the source plane is then built through a standard ray-tracing method. The  
 612 resulting pattern is shown in Extended Data Figure 6.

613 To measure the fluctuations over time, we assume the star is moving at a velocity  $v = 1000 \text{ km s}^{-1} \sim$   
 614  $0.001 \text{ pc/yr}$  relative to the caustic network<sup>3;73</sup>. This velocity estimate accounts for rotation of the  
 615 lensed galaxy, motions of stars and galaxies within the cluster lens, and relative transverse velocities  
 616 between the cluster lens, lensed galaxy, and Earth with respect to the Hubble flow. Windhorst et al.<sup>67</sup>  
 617 test whether  $1000 \text{ km s}^{-1}$  is reasonable by adding random space motions of up to several thousand  
 618  $\text{km s}^{-1}$  to well-studied clusters and measuring the effect on the cluster redshift space distributions,

619 finding velocities of  $\sim 1000 \text{ km s}^{-1}$  do not distort the observed cluster properties. Thus we infer  
 620 that this velocity is reasonable in our case. Ultimately, the exact velocity assumed will impact only  
 621 the duration and frequency of microlensing events, with little to no effect on their amplitude. The  
 622 direction the star moves relative to the caustic network also impacts the expected variability in  
 623 magnification. If the star were moving perpendicular to the cluster caustic, we would expect the  
 624 greatest variation in time, whereas if the star were to move parallel to the cluster caustic we expect  
 625 much less variation. For our analysis, we assume the star is moving at an angle of  $45^\circ$  relative to  
 626 the cluster caustic. This will produce moderate fluctuations in time, with the star typically staying  
 627 within a factor of two of our measured brightness. As with the velocity, the direction will only impact  
 628 the duration and frequency of magnification fluctuations. Because we are in a microlensing regime  
 629 with a larger effective optical depth ( $> 1$ ), microcaustics will overlap and limit the amplitude of  
 630 variations as the star traverses this caustic network. Thus no matter what velocity and direction we  
 631 assume, the star will most likely stay within a factor of two of its current magnification, matching  
 632 our observations.

633 Extended Data Figure 6 shows simulated light curves and likelihoods for both microlensing stellar  
 634 densities  $\Sigma_* = 1$  and  $10 M_\odot \text{pc}^{-2}$ . The higher stellar density reduces the variability in flux as the  
 635 microlensing caustic network saturates, yielding a consistently high magnification  $2\mu \sim 9000$ . In  
 636 this case, we can expect with  $\sim 65\%$  confidence that magnifications measured 3.5 years apart will  
 637 be within a factor of 1.4, as observed. If the stellar density is lower ( $1 M_\odot \text{pc}^{-2}$ ), this likelihood  
 638 decreases to  $\sim 40\%$ , which is still fairly likely. Therefore, both of these predictions are consistent with  
 639 our observations.

640 We also tested a third “critical” scenario with maximal time variations and found these very similar  
 641 to the results for  $\Sigma_* = 1 M_\odot \text{pc}^{-2}$ . The degree of variability depends on the product  $\mu\Sigma_*$ . Our  
 642 simulations had  $\mu\Sigma_* = 44800$ ,  $4480$ , and finally  $1600$  for the critical case. Tighter constraints on *both*  
 643 parameters  $\mu$  and  $\Sigma_*$  are required to improve variability predictions. Future observations will better  
 644 constrain these parameters while providing better data on variability or lack thereof. An approved

645 upcoming *HST* program (GO 16668; PI Coe) will add time monitoring observations to test these  
 646 predictions and more precisely constrain the baseline flux.

### 647 2.7. Luminosity and Stellar Constraints

648 From our magnification measurements of  $\mu = 1000 - 40000$  derived above, and Earendel’s observed  
 649 flux  $49 \pm 4$  nJy in the *HST* F110W filter ( $0.9 - 1.4 \mu\text{m}$ ), we calculate a delensed flux of  $1 - 50$  pJy,  
 650 corresponding to an AB magnitude of  $38.7 - 34.7$ . This then gives an absolute UV ( $1600\text{\AA}$ ) magnitude  
 651 of  $-8 < M_{AB} < -12$ , given the distance modulus  $48.9$  at  $z = 6.2$  and flux per unit frequency dimming  
 652 by  $1 + z$  ( $2.1$  mag). We can then calculate the intrinsic stellar luminosity, assuming blackbody spectra  
 653 for hot stars with effective temperatures  $T_{\text{eff}} > 40000$  K. For cooler stars, we used the lowest surface  
 654 gravity models available from the grid of empirically-corrected  $[\text{M}/\text{H}] = -1$  stellar atmosphere spectra  
 655 compiled by Lejeune et al.<sup>54</sup>. This yields the black tracks in Figure 3 for a given magnification and  
 656 delensed flux. Green shaded regions show magnification uncertainties (factor of 7 for each individual  
 657 lens model); the photometric uncertainties are 10% (insignificant and thus not included). We also  
 658 explored the effects of different metallicity stellar atmosphere models (from  $[\text{M}/\text{H}] = 0$  to  $-5$  using  
 659 Lejeune et al.<sup>54</sup>), and found  $\Delta \log L < 0.1$  for  $T_{\text{eff}} > 10000$  K, and  $\Delta \log L \sim 0.2$  for  $T_{\text{eff}} < 10000$   
 660 K, which is insignificant compared to our other uncertainties. The redshifted spectrum of a B-type  
 661 star with temperature  $\sim 20000 - 30000$  K maximizes the flux in the F110W filter, whereas spectra of  
 662 hotter / cooler stars require a higher total bolometric luminosity to produce the same F110W flux.  
 663 For our calculations of the stellar luminosity, we assume zero extinction due to interstellar dust.  
 664 With current data, we cannot robustly estimate the extinction around the star. While BAGPIPES  
 665 yields an estimate of  $A_V = 0.15 \pm 0.1$  mag for the full galaxy, we would expect less dust in the ISM  
 666 near the outskirts of the galaxy where we see the star. On the other hand, we would expect this  
 667 massive star to still be associated with a star forming region, which would increase the expected dust  
 668 extinction. To get a rough estimate of the effect of dust, we can assume we have  $E(B - V) \sim 0.1$   
 669 mag in the region surrounding the star (reasonable for a star cluster in a low-metallicity galaxy<sup>55</sup>),  
 670 and an SMC-like extinction law with  $R_V \sim 2.93$ . With these assumptions, we would expect a factor

671  $\sim 2$  reduction in flux. This would lead to an equivalent increase in the inferred luminosity. While  
 672 this is significant, it is still far less than the large magnification uncertainty.

673 In Figure 3, we show low-metallicity ( $0.1Z_{\odot}$ ) dwarf galaxy predictions from BoOST, as may roughly  
 674 be expected at  $z \sim 6$  based on simulations<sup>32</sup>. There is considerable scatter in galaxy metallicities in  
 675 both observations and simulations. Additionally, the star is not necessarily at the same metallicity as  
 676 the galaxy overall. To probe the effects of metallicity on our interpretation of the mass of Earendel,  
 677 we consider a range of stellar tracks from BoOST with varying metallicities. These range from solar  
 678 metallicity  $Z_{\odot}$  down to  $0.004Z_{\odot}$ , the full range available from BoOST models. These tracks, along  
 679 with a green shaded band showing our full luminosity uncertainty across all lens models, is shown  
 680 in Extended Data Figure 7. The differences between various low-metallicity tracks are small relative  
 681 to our current uncertainties, so the exact choice of metallicity does not impact our conclusions; we  
 682 still find massive stars best match our constraints. A more important uncertainty is in the stellar  
 683 modeling of massive stars, which radiate near the Eddington limit. In such stars, the expansion of  
 684 their outer layers is poorly understood, leading to increased uncertainty on predictions of stellar radii  
 685 and effective temperatures<sup>56</sup>. The luminosity of the star is not impacted by this uncertainty, so these  
 686 models still provide a useful estimate of the mass of the star.

687 In Extended Data Figure 8, we show the BoOST  $0.1Z_{\odot}$  stellar evolution tracks vs. time. We see that  
 688 very massive stars of  $100M_{\odot}$  or more spend the greatest time ( $\sim 2$  Myr) with a luminosity matching  
 689 Earendel within the uncertainties. The next less massive track  $\sim 55M_{\odot}$  would only match our  
 690 luminosity constraint for  $\sim 0.5$  Myr. This shorter time would decrease the probability of observing  
 691 such a star by  $\sim 1/4$ . On the other hand, lower mass  $55M_{\odot}$  stars may be roughly 4 times as numerous  
 692 as  $100M_{\odot}$  stars, depending on the IMF. From this simple analysis, we estimate that Earendel's light  
 693 may be most likely generated by a star with  $\sim 50 - 100M_{\odot}$ . More massive stars are less likely  
 694 because they are less numerous, while a less massive star would not be bright enough. Given the  
 695 large uncertainties on our observational constraints, we leave more detailed analysis of lifetimes,  
 696 formation rates, and magnification probabilities for future work.

697 Such massive stars are rarely single<sup>28;29</sup>. Multiple less massive stars could also combine to produce  
 698 the observed luminosity. While it is most likely that a single star will dominate the light in such a  
 699 system, there is a possibility of finding tightly bound multiple systems of similar masses, and thus  
 700 similar brightnesses. El-Badry et al.<sup>57</sup> find a sharp excess of “twin” systems, with a mass ratio  
 701  $\gtrsim 0.95$  indicating that the stars are roughly equal masses. This analysis was restricted to lower  
 702 mass stars, but Moe & Di Stefano<sup>30</sup> find a similar (although more modest) excess for more massive  
 703 systems. Additionally, Moe & Di Stefano<sup>30</sup> find that the fraction of stars in triple and quadruple  
 704 systems increases as the primary star’s mass increases, up to a quadruple fraction of  $\sim 50\%$  for stars  
 705 of mass  $\sim 25M_{\odot}$ . In any case of a twin/triple/quadruple star, the contribution from companion  
 706 stars becomes non-negligible. This would effectively reduce the inferred mass of the primary star,  
 707 potentially down to  $\sim 20M_{\odot}$  in the case of a quadruple system of equal mass main sequence stars.  
 708 We note that multiple bright stars would also dampen microlensing variations, as one star may be  
 709 crossing a microcaustic while others are not, further supporting our observation of relatively stable  
 710 flux.

711 With the *HST* photometry available, we cannot reliably distinguish between different stellar types  
 712 and effective temperatures, and thus stellar mass. We have multi-band imaging, but only the F110W  
 713 band has a reliable ( $> 5\sigma$  significance) detection. Other WFC3-IR bands do detect the star, but  
 714 at much lower significance, the highest being F160W with a  $\sim 3\sigma$  detection. Additionally, these  
 715 other IR bands were taken in the original RELICS imaging. The 3.5 year gap between observations  
 716 provides ample time for the magnification to vary considerably. Our microlensing analysis suggests  
 717 that the magnification will stay high ( $\mu \geq 1000$ ) for many years, but fluctuations of a factor of 2 are  
 718 expected.

719 ACS/F814W imaging was obtained in every epoch of observations, however the stacked detection in  
 720 this band is still only at  $4.4\sigma$  confidence. Additionally, this bandpass spans the Lyman- $\alpha$  break at  
 721  $z \sim 6$ , so the F814W flux is primarily a function of redshift: more flux drops out as redshift increases  
 722 up to  $z = 7$ . Any SED constraint from *HST* photometry would be weak. Future spectroscopic

723 observations with our approved JWST program (GO 2282; PI Coe) will determine the type and  
 724 temperature of this star, placing it on the H-R diagram.

### 725 2.8. Probability of Observing a Massive Star

726 In the following, we assess the probability of observing a lensed star with  $M_* \gtrsim 100M_\odot$  at sufficiently  
 727 high magnification to be detected in our data. To do so, we use our model of the Sunrise Arc  
 728 to estimate the total star formation rate (SFR) of the host galaxy within a region close to the  
 729 lensing caustic, and use assumptions on the stellar IMF to convert this into an estimate on the  
 730 number of high-mass stars within this area. Using the formalism presented by Diego<sup>18</sup>, and fitting  
 731 for necessary constants using our LTM lens model, we calculate a source plane area of  $\sim 500 \text{ pc}^2$   
 732 ( $\sim 0.5 \text{ pc}$  perpendicular to the caustic times  $\sim 1000 \text{ pc}$  along the caustic) that intersects the host  
 733 galaxy at a magnification of  $2\mu \gtrsim 4200$  (set by the minimum magnification to detect a  $M_* \sim 100 M_\odot$   
 734 star in our data). We next estimate the surface brightness of the arc close to the location of the  
 735 star, finding  $I \sim 6 \times 10^{-6} \text{ nJy pc}^{-2}$ . By assuming that the surface brightness of the host galaxy  
 736 remains approximately constant along the caustic, we may then convert surface brightness to total  
 737 SFR within the  $2\mu > 4200$  region that intersects the host galaxy. Using Starburst99 v.7.0.1<sup>58</sup> under  
 738 the assumption of a Kroupa<sup>59</sup> IMF throughout the  $0.01\text{--}120 M_\odot$  interval and a constant-SFR stellar  
 739 population with  $Z = 0.001$  at age 100 Myr, we find a total  $SFR \sim 2 \times 10^{-4} M_\odot \text{ yr}^{-1}$  in the host  
 740 galaxy region magnified by  $2\mu > 4200$ .

741 We next calculate the probability of observing a star of mass  $\geq 100 M_\odot$  at this SFR. This is done with  
 742 two star formation prescriptions, one assuming clustered star formation wherein stars are distributed  
 743 into star clusters with a cluster mass function  $dN_{\text{cluster}}/dM_{\text{cluster}} \propto M_{\text{cluster}}^{-2}$  between  $20 - 10^7 M_\odot$ ,  
 744 then randomly sampled from the IMF with the limit  $M_* < M_{\text{cluster}}$  using the SLUG v2.0 code<sup>60;61</sup>.  
 745 This tends to result in fewer high mass stars. The other possibility is unclustered star formation,  
 746 in which stars are randomly sampled from the IMF without first being split into clusters. This  
 747 method results in a greater proportion of massive stars. From this calculation, we find a probability  
 748  $P(\geq 100M_\odot) \sim 2\%$  in the clustered scenario, and  $\sim 4\%$  in the unclustered scenario.



749 From this calculation, we conclude that one might expect to find such a massive, lensed star in about  
 750 1 in 25–50 such caustic crossing galaxies. Tens of galaxies like this have been observed in *HST* images  
 751 from various programs. Therefore, the probability of such a discovery is reasonable.

752 We note that a different choice of IMF over the stated mass range could impact the calculated SFR,  
 753 up to a factor  $\sim 1.5$  if we were to use the Salpeter<sup>45</sup> IMF<sup>62</sup>. However, this change will be largely  
 754 canceled out by the lower probability per unit stellar mass of forming  $> 100M_{\odot}$  stars using the  
 755 Salpeter IMF. The difference if we were to use a Chabrier<sup>63</sup> IMF would be even smaller, as that is  
 756 more similar to the Kroupa IMF over our mass range. Ultimately, any uncertainty introduced by the  
 757 choice of IMF will be sub-dominant compared to other assumptions, such as the assumed metallicity.  
 758 However, if the stellar IMF would be more top-heavy than the Kroupa IMF (i.e., contain a larger  
 759 fraction of massive stars), as has been argued to be the case for star formation in low-metallicity  
 760 environments<sup>64</sup>, then the probability for detecting a  $\geq 100 M_{\odot}$  star could be significantly higher.  
 761 The probability would also increase in scenarios where the host galaxy, despite being metal-enriched,  
 762 contains a fraction of Pop III stars, as in the simulations by Sarmiento et al.<sup>65;66</sup>. From the MESA  
 763 mass-luminosity relation of such stars, Windhorst et al.<sup>67</sup> showed that most of their light comes from  
 764  $20 - 200 M_{\odot}$  stars, so that finding a single  $\sim 100 M_{\odot}$  star during a significant caustic magnification  
 765 is possible.

### 766 2.9. *Alternative Possibilities*

767 There are a few alternative possibilities we consider for this object. One such possibility is that  
 768 Earendel is a Population III star with zero metallicity. Calculations of observable properties of Pop  
 769 III stars from MESA stellar evolution models show that a  $> 50M_{\odot}$  in a hydrogen-depleted phase would  
 770 match our delensed flux constraint, as would a ZAMS star of  $> 300M_{\odot}$ <sup>67</sup>.

771 The lifetime of a massive Pop III star would be short relative to its host galaxy. It would therefore  
 772 require a pristine zero-metallicity environment within the host galaxy to form. Such regions become  
 773 less common as more early generation stars explode and enrich their surroundings with heavier  
 774 elements. Our SED fitting of the Sunrise Arc gives a stellar mass of  $M_{*} \sim 3 \times 10^7 M_{\odot}$ , from which  
 775 we might expect a metallicity on the order of  $0.01Z_{\odot}$  or  $0.1Z_{\odot}$ <sup>32</sup>. This non-zero metallicity would

776 indicate that some enrichment has taken place. Even if we assume the galaxy overall has been  
 777 enriched, finding a Pop III stellar population is not ruled out. Some models predict that pockets of  
 778 zero-metallicity gas (from which Pop III stars can form) may still exist at  $z \sim 6$ , particularly near  
 779 the outskirts of galaxies<sup>74</sup>. Observationally, Vanzella et al.<sup>75</sup> report a strongly lensed star cluster  
 780 consistent with being a complex of Pop III stars at  $z = 6.6$ . In this case, pockets of zero-metallicity  
 781 stars may exist in otherwise metal enriched galaxies. Spectroscopic follow-up will be required to  
 782 assess the possibility of Earendel being a Pop III star.

783 Although the probability of Earendel being a zero-metallicity Pop III star is low, if it turns out to be  
 784 such an object it would be the first such star observed. This would provide important confirmation  
 785 that such stars formed, and would offer an incredible opportunity to study one in detail. Furthermore,  
 786 such a star is a possible progenitor for the recently observed binary black hole merger GW190521,  
 787 which is too massive to be explained by standard stellar remnants<sup>76</sup>. Recent studies<sup>77;78</sup> have proposed  
 788 that extremely metal poor or zero metallicity stars are viable progenitors for this event. Finding such  
 789 a star would offer a chance to study it in detail and refine models of how these stars collapse into  
 790 black holes.

791 Another possibility is that this object is an accreting stellar mass black hole. If the black hole were  
 792 persistently fed by a lower mass star overflowing its Roche lobe, it could continue to shine up to  
 793 60 Myr<sup>67</sup>. Note we assume this would be a persistent source. A transient outburst, which would  
 794 shine for weeks to months<sup>79</sup>, would be ruled out by the lack of variation observed (see §2.3). A  
 795 stellar mass black hole accretion disk would have strong X-ray emission, whereas a star would not.  
 796 Following the multicolor accretion disk model in Windhorst et al.<sup>67</sup>, a  $200M_{\odot}$  black hole formed from  
 797 a  $\sim 300M_{\odot}$  Pop III star would have an inner accretion disk with  $T_{max} \sim 7.7 \text{ keV} \sim 3 \times 10^7 \text{ K}$ . Most  
 798 of the X-ray emission would originate near the center of the disk, from radii around a few times  
 799 the Schwarzschild radius ( $\gtrsim 900\text{--}1800 \text{ km}$ ). The maximum possible magnification of the tiny X-ray  
 800 emitting region could then be substantially (perhaps  $100\times$ ) larger than that for the rest-frame UV  
 801 stellar light, or  $\mu \gtrsim 10^6$ . Most of the remainder of the accretion disk would shine in the rest-frame  
 802 UV at the Eddington limit with very similar size, luminosity, and surface brightness as a massive

803 star. Hence, a stellar mass black hole accretion disk would appear very similar in the HST images  
 804 to a massive star. Analysis of archival X-ray data from XMM-Newton showed no clear signal near  
 805 this position, supporting the stellar interpretation. We note, however, that the 6'' spatial resolution  
 806 of XMM-Newton would dilute the signal from such a black hole accretion disk. Deeper, higher-  
 807 resolution X-ray images with the Chandra X-ray Observatory (resolution  $\sim 0.5''$ ) or the upcoming  
 808 Athena mission could conclusively determine if this source is a black hole.

809 We also consider the possibility that this object is not associated with the Sunrise Arc, and thus  
 810 not a lensed star at  $z \sim 6$ . The first possibility would be a local star which happens to align with  
 811 the background arc. While possible, this is unlikely given the exact alignment of the object with  
 812 the background arc. Holwerda et al.<sup>80</sup> found  $\sim 1.2$  M-type dwarfs per arcmin<sup>2</sup> out to magnitude  
 813 24 in their analysis of multiple fields observed with HST. Rescaling to 27th magnitude, we estimate  
 814 we might observe of order  $\sim 100$  such stars per arcmin<sup>2</sup> in our observations. Given the small solid  
 815 angle surrounding the critical curve crossings in the Sunrise Arc (constrained to within 0.1''), the  
 816 probability of one of these local dwarfs aligning with both the arc and critical curve by chance is of  
 817 order 0.01%. If Earendel were a local brown dwarf, we might see some evidence of proper motion over  
 818 the 3.5 year observation window. We see no evidence of motion, strengthening the interpretation that  
 819 this star is associated with the Sunrise Arc. We note that we cannot conclusively rule out a brown  
 820 dwarf based on existing *HST* photometry. We fit the SED of Earendel alone to brown dwarf spectra  
 821 from the SpeX Prism Library<sup>81</sup>, and find that a 3000 K local star could reproduce our observations.  
 822 We expect upcoming *JWST* photometry and spectroscopy to rule out a brown dwarf conclusively.  
 823 For now, we rely on the unlikely chance alignment and lack of proper motion to disfavor a local brown  
 824 dwarf.

825 Other possibilities to consider for this object are distinct galaxies in the foreground, cluster, or lensed  
 826 background. But even analyzed independently, Earendel's photometric redshift is the same as the  
 827 full galaxy:  $z = 6.2 \pm 0.1$  (95% CL) with negligible likelihood at lower redshifts according to BPZ  
 828 given the Lyman break, which is clear even in this faint object. Furthermore, any foreground / lensed  
 829 background galaxy would most likely appear larger and spatially resolved in the *HST* images. Note

830 a  $z < 6$  background galaxy, say at  $z \sim 2$ , would not be on the lensing critical curve for that redshift,  
 831 but it would still be magnified by a factor of a few to perhaps tens, requiring a small galaxy to not  
 832 appear spatially resolved when magnified. A quasar would still appear point-like when lensed, but  
 833 of course quasars are less numerous and we would expect a redder rest-frame ultraviolet continuum  
 834 slope<sup>82</sup>. Again, we expect upcoming to *JWST* observations to spectroscopically confirm Earendel is  
 835 a star at  $z \sim 6.2$  within the Sunrise Arc galaxy.

### 836 3. DATA AVAILABILITY

837 All *HST* image data used in this analysis are publicly available on the Mikulski Archive for Space  
 838 Telescopes (MAST), and can be found through the following DOI hyperlinks: [RELICS](#), and follow-up  
 839 [HST GO 15842](#).

### REFERENCES

- 840 [33]Wen, Z. L., Han, J. L. & Liu, F. S. A Catalog of 132684 Clusters of Galaxies Identified from Sloan Digital  
 841 Sky Survey III. *Astrophys. J. Suppl.* **199**, 34 (2012).
- 842 [34]Wen, Z. L. & Han, J. L. Calibration of the Optical Mass Proxy for Clusters of Galaxies and an Update of  
 843 the WHL12 Cluster Catalog. *Astrophys. J.* **807**, 178 (2015).
- 844 [35]Alam, S. *et al.* The Eleventh and Twelfth Data Releases of the Sloan Digital Sky Survey: Final Data from  
 845 SDSS-III. *Astrophys. J. Suppl.* **219**, 12 (2015).
- 846 [36]Planck Collaboration *et al.* Planck 2015 results. XXVII. The second Planck catalogue of  
 847 Sunyaev-Zeldovich sources. *Astron. Astrophys.* **594**, A27 (2016).
- 848 [37]Sunyaev, R. A., & Zeldovich, Y. B. Small-Scale Fluctuations of Relic Radiation. *Ap&SS* **7**, 3-19 (1970).
- 849 [38]Strait, V. *et al.* RELICS: Properties of  $z \geq 5.5$  Galaxies Inferred from Spitzer and Hubble Imaging,  
 850 Including A Candidate  $z \sim 6.8$  Strong [OIII] emitter. *Astrophys. J.* **910**, 135 (2021).
- 851 [39]Bertin, E. & Arnouts, S. SExtractor: Software for source extraction. *Astron. Astrophys. Suppl.* **117**,  
 852 393-404 (1996).
- 853 [40]Beintez, N. Bayesian Photometric Redshift Estimation. *Astrophys. J.* **536**, 571-583 (2000).
- 854 [41]Coe, D. *et al.* Galaxies in the Hubble Ultra Deep Field. I. Detection, Multiband Photometry, Photometric  
 855 Redshifts, and Morphology. *Astron. J.* **132**, 926-959 (2006).

- 856 [42]Carnall, A. C., McLure, R. J., Dunlop, J. S. & Davé, R. Inferring the star formation histories of massive  
857 quiescent galaxies with BAGPIPES: evidence for multiple quenching mechanisms. *Mon. Not. R. Astron.*  
858 *Soc.* **480**, 4379-4401 (2018).
- 859 [43]Eldridge, J. J. *et al.* Binary Population and Spectral Synthesis Version 2.1: Construction, Observational  
860 Verification, and New Results. *PASA* **34**, e058 (2017).
- 861 [44]Ferland, G. J. *et al.* The 2017 Release Cloudy. *RMxAA* **53**, 385-438 (2017).
- 862 [45]Salpeter, E. E. The Luminosity Function and Stellar Evolution. *Astrophys. J.* **121**, 161 (1955).
- 863 [46]Calzetti, D. *et al.* The Dust Content and Opacity of Actively Star-forming Galaxies. *Astrophys. J.* **533**,  
864 682-695 (2000).
- 865 [47]Ellis, R. S. *et al.* The Homogeneity of Spheroidal Populations in Distant Clusters. *Astrophys. J.* **483**,  
866 582-596 (1997).
- 867 [48]Stanford, S. A., Eisenhardt, P. R. & Dickinson, M. The Evolution of Early-Type Galaxies in Distant  
868 Clusters. *Astrophys. J.* **492**, 461-479 (1998).
- 869 [49]Hastings, W. K. Monte Carlo sampling methods using Markov chains and their applications. *Biometrika*  
870 **57**, 97-109 (1970).
- 871 [50]Limousin, M., Kneib, J.-P. & Natarajan, P. Constraining the mass distribution of galaxies using  
872 galaxy-galaxy lensing in clusters and in the field. *Mon. Not. R. Astron. Soc.* **356**, 309-322 (2005).
- 873 [51]Eliasdóttir, Á. *et al.* Where is the matter in the Merging Cluster Abell 2218? *arXiv e-prints*,  
874 arXiv:0710.5636 (2007).
- 875 [52]Navarro, J. F., Frenk, C. S. & White, S. D. M. The Structure of Cold Dark Matter Halos. *Astrophys. J.*  
876 **462**, 563 (1996).
- 877 [53]Johnson, T. L. *et al.* Star Formation at  $z = 2.481$  in the Lensed Galaxy SDSS J1110+6459. I. Lens  
878 Modeling and Source Reconstruction. *Astrophys. J.* **843**, 78 (2017).
- 879 [54]Lejeune, T., Cuisinier, F. & Buser, R. Standard stellar library for evolutionary synthesis. I. Calibration of  
880 theoretical spectra. *Astron. Astrophys. Suppl.* **125**, 229-246 (1997).
- 881 [55]Calzetti, D. *et al.* The Brightest Young Star Clusters in NGC 5253. *Astrophys. J.* **811**, 75 (2015).
- 882 [56]Sanyal, D., Grassitelli, L., Langer, N. & Bestenlehner, J. M. Massive main-sequence stars evolving  
883 at924the Eddington limit. *Astron. Astrophys.* **580**, A20 (2015).
- 884 [57]El-Badry, K., Rix, H.-W., Tian, H., Duchêne, G. & Moe, M. Discovery of an equal-mass ‘twin’ binary  
885 population reaching 1000 + au separations. *Mon. Not. R. Astron. Soc.* **489**, 5822-5857 (2019).
- 886 [58]Leitherer, C. *et al.* Starburst99: Synthesis Models for Galaxies with Active Star Formation. *Astrophys. J.*  
887 *Suppl.* **123**, 3-40 (1999).

- 888 [59]Kroupa, P. On the variation of the initial mass function. *Mon. Not. R. Astron. Soc.* **322**, 231-246 (2001).
- 889 [60]da Silva, R. L., Fumagalli, M. & Krumholz, M. SLUG—Stochastically Lighting Up Galaxies. I. Methods  
890 and Validating Tests. *Astrophys. J.* **745**, 145 (2012).
- 891 [61]Krumholz, M. R., Fumagalli, M., da Silva, R. L., Rendahl, T. & Parra, J. SLUG – stochastically lighting  
892 up galaxies - III. A suite of tools for simulated photometry, spectroscopy, and Bayesian inference with  
893 stochastic stellar populations. *Mon. Not. R. Astron. Soc.* **452**, 1447-1467 (2015).
- 894 [62]Madau, P. & Dickinson, M. Cosmic Star-Formation History. *Annu. Rev. Astron. Astrophys.* **52**, 415-486  
895 (2014).
- 896 [63]Chabrier, G. Galactic Stellar and Substellar Initial Mass Function. *PASP* **115**, 763-795 (2003).
- 897 [64]Kehrig, C. *et al.* The extended He II  $\lambda$ 4686 emission in the extremely metal-poor galaxy SBS 0335 - 052E  
898 seen with MUSE. *Mon. Not. R. Astron. Soc.* **480**, 1081-1095 (2018).
- 899 [65]Sarmiento, R., Scannapieco, E. & Cohen, S. Following the Cosmic Evolution of Pristine Gas. II. The Search  
900 for Pop III-bright Galaxies. *Astrophys. J.* **854**, 75 (2018).
- 901 [66]Sarmiento, R., Scannapieco, E. & Côté, B. . Following the Cosmic Evolution of Pristine Gas. III. The  
902 Observational Consequences of the Unknown Properties of Population III Stars. *Astrophys. J.* **871**, 206  
903 (2019).
- 904 [67]Windhorst, R. A. *et al.* On the Observability of Individual Population III Stars and Their Stellar-mass  
905 Black Hole Accretion Disks through Cluster Caustic Transits. *Astrophys. J. Suppl.* **234**, 41 (2018).
- 906 [68]Dai, L. & Pascale, M. New Approximation of Magnification Statistics for Random Microlensing of  
907 Magnified Sources. *arXiv e-prints*, arXiv:2104.12009 (2021).
- 908 [69]Jiménez-Teja, Y. *et al.* RELICS: ICL Analysis of the  $z = 0.566$  merging cluster WHL J013719.8-08284.  
909 *arXiv e-prints*, arXiv:2109.04485 (2021).
- 910 [70]Kriek, M. *et al.* An Ultra-Deep Near-Infrared Spectrum of a Compact Quiescent Galaxy at  $z =$   
911  $2.2$ . *Astrophys. J.* **700**, 221-231 (2009).
- 912 [71]Bruzual, G. & Charlot, S. Stellar population synthesis at the resolution of 2003. *Mon. Not. R. Astron.*  
913 *Soc.* **344**, 1000-1028 (2003).
- 914 [72]Spera, M., Mapelli, M. & Bressan, A. The mass spectrum of compact remnants from the PARSEC stellar  
915 evolution tracks.
- 916 [73]Oguri, M., Diego, J. M., Kaiser, N., Kelly, P. L. & Broadhurst, T. Understanding caustic crossings in giant  
917 arcs: Characteristic scales, event rates, and constraints on compact dark matter. *Phys. Rev. D* **97**,  
918 023518 (2018).

- 919 [74]Trenti, M., Stiavelli, M. & Shull, J. M. Metal-free Gas Supply at the Edge of Reionization: Late-epoch  
920 Population III Star Formation. *Astrophys. J.* **700**, 1672-1679 (2009).
- 921 [75]Vanzella, E. *et al.* Candidate Population III stellar complex at  $z = 6.629$  in the MUSE Deep Lensed Field.  
922 *Mon. Not. R. Astron. Soc.* **494**, L81-L85 (2020).
- 923 [76]Abbott, R. *et al.* GW190521: A Binary Black Hole Merger with a Total Mass of  $150M_{\odot}$ . *Phys. Rev. Lett.*  
924 **125**, 101102 (2020).
- 925 [77]Farrell, E. *et al.* Is GW190521 the merger of black holes from the first stellar generations? *Mon. Not. R.*  
926 *Astron. Soc. Lett.* **502**, L40-L44 (2020).
- 927 [78]Kinugawa, T., Nakamura, T. & Nakano, H. Formation of binary black holes similar to GW190521 with a  
928 total mass of  $150M_{\odot}$  from Population III binar star evolution. *Mon. Not. R. Astron. Soc. Lett.* **501**,  
929 L49-L53 (2020).
- 930 [79]Zdziarski, A. A. & Gierliński, M. Radiative Processes, Spectral States and Variability of Black-Hole  
931 Binaries. *Progress of Theoretical Physics Supplement* **155**, 99-119 (2004).
- 932 [80]Holwerda, B. W. *et al.* Milky Way Red Dwarfs in the BoRG Survey; Galactic Scale-height and the  
933 Distribution of Dwarf Stars in WFC3 Imaging. *Astrophys. J.* **788**, 77 (2014).
- 934 [81]Burgasser, A. J. & Splat Development Team. The SpeX Prism Library Analysis Toolkit (SPLAT): A Data  
935 Curation Model. *Astronomical Society of India Conference Series* **14**, 7-12 (2017).
- 936 [82]Hainline, K. N., Shapley, A. E., Greene, J. E. & Steidel, C. C. The Rest-frame Ultraviolet Spectra of  
937 UV-selected Active Galactic Nuclei at  $z \sim 2-3$ . *Astrophys. J.* **733**, 31 (2011).

## 4. ACKNOWLEDGEMENTS

The RELICS Hubble Treasury Program (GO 14096) and follow-up program (GO 15842) consist of observations obtained by the NASA/ESA *Hubble Space Telescope (HST)*. Data from these *HST* programs were obtained from the Mikulski Archive for Space Telescopes (MAST), operated by the Space Telescope Science Institute (STScI). Both *HST* and STScI are operated by the Association of Universities for Research in Astronomy, Inc. (AURA), under NASA contract NAS 5-26555. The *HST* Advanced Camera for Surveys (ACS) was developed under NASA contract NAS 5-32864.

JMD acknowledges the support of project PGC2018-101814-B-100 (MCIU/AEI/MINECO/FEDER, UE) and María de Maeztu, ref. MDM-2017-0765.

AZ acknowledges support from the Ministry of Science & Technology, Israel.

RAW acknowledges support from NASA JWST Interdisciplinary Scientist grants NAG5-12460, NNX14AN10G and 80NSSC18K0200 from GSFC.

EZ and AV acknowledge funding from the Swedish National Space Board.

MO acknowledges support from World Premier International Research Center Initiative, MEXT, Japan, and JSPS KAKENHI Grant Number JP20H00181, JP20H05856, JP18K03693.

GM received funding from the European Union's Horizon 2020 research and innovation programme under the Marie Skłodowska-Curie grant agreement No MARACAS - DLV-896778.

PLK acknowledges support from NSF AST-1908823.

Y. J-T acknowledges financial support from the European Union's Horizon 2020 research and innovation programme under the Marie Skłodowska-Curie grant agreement No 898633, and from the State Agency for Research of the Spanish MCIU through the "Center of Excellence Severo Ochoa" award to the Instituto de Astrofísica de Andalucía (SEV-2017-0709).

S.T. acknowledges The Cosmic Dawn Center of Excellence is funded by the Danish National Research Foundation under grant No. 140.

## 5. AUTHOR INFORMATION

## 5.1. Contributions



964 B.W. identified the star, led the lens modeling and size constraint analysis, and wrote the majority  
965 of the manuscript. D.C. proposed and carried out observations, measured photometry and redshifts,  
966 and helped analyze size and magnification constraints. J.M.D. performed and analyzed microlensing  
967 simulations, and contributed to lens model analysis. A.Z., G.M., M.O., and K.S. contributed to the  
968 lens model analyses. E.Z. calculated stellar constraints based on observed magnitude and magnifica-  
969 tion. P.D. and Y.J.-T. calculated stellar surface mass densities used in microlensing analysis. P.K.  
970 and R.W. helped compare results and methods to previous lensed star detections and theoretical  
971 predictions. F.X.T., S.E.d.M., and A.V. contributed to stellar constraint analysis and interpretation.  
972 R.J.A. reduced the HST images. M.B. and V.S. obtained and analyzed Spitzer data. All authors  
973 contributed to the scientific interpretation of the results and to aspects of the analysis and writing.

974 *5.2. Corresponding author*

975 Correspondence to Brian Welch: [bwelch7@jhu.edu](mailto:bwelch7@jhu.edu).

## 976 6. ETHICS DECLARATIONS

### 977 **Competing Interests**

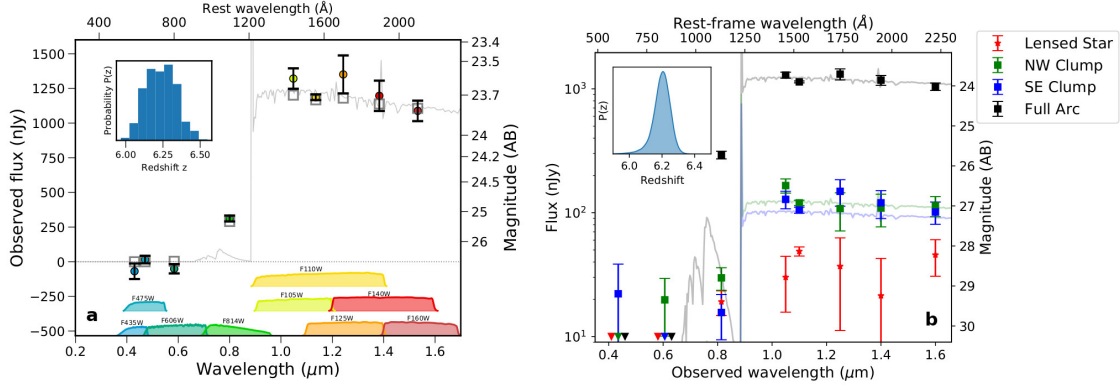
978 The authors declare no competing interests.

Camera	Filter	HST GO 14096	HST GO 15842	Depth $5\sigma$	Sunrise Arc	Earendel
		Exposure Time (s)	Exposure Time (s)	(AB mag)	Flux (nJy)	Flux (nJy)
ACS	F435W	2072		27.2	$-69 \pm 56$	$-8 \pm 12$
ACS	F475W		3988	27.9	$16 \pm 27$	$9 \pm 6$
ACS	F606W	2072		27.6	$-51 \pm 33$	$-2 \pm 7$
ACS	F814W	2243	11083	28.0	$312 \pm 21$	$19 \pm 4$
WFC3/IR	F105W	1411		26.7	$1321 \pm 74$	$30 \pm 14$
WFC3/IR	F110W		5123	27.7	$1187 \pm 21$	$49 \pm 4$
WFC3/IR	F125W	711		26.0	$1351 \pm 137$	$37 \pm 26$
WFC3/IR	F140W	711		26.2	$1197 \pm 109$	$21 \pm 21$
WFC3/IR	F160W	1961		26.5	$1088 \pm 74$	$46 \pm 15$

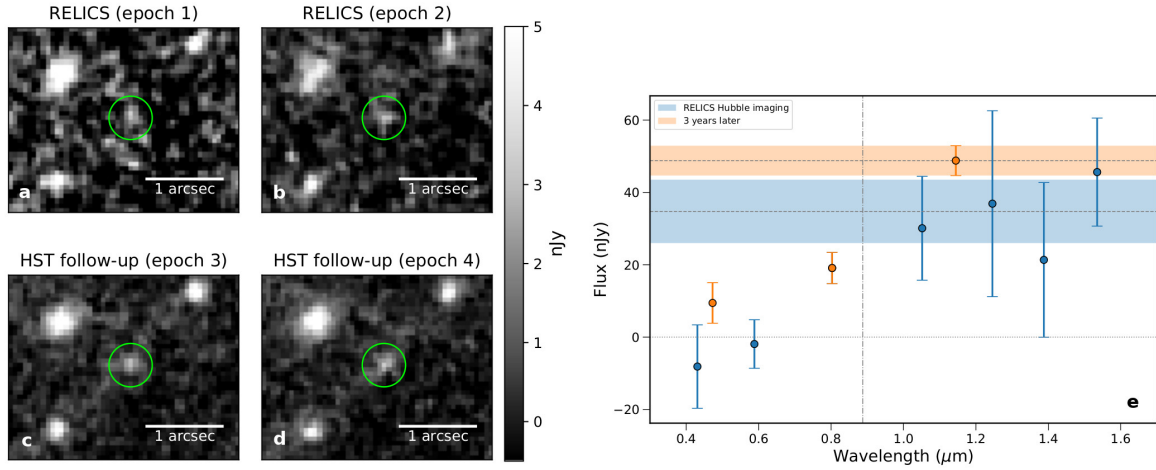
**Extended Data Table 1.** Hubble imaging of WHL0137-08 in nine filters and photometry measured for the Sunrise Arc and Earendel. Imaging was obtained by RELICS (HST GO 14096) and follow-up imaging 3.5 years later (HST GO 15842). Final  $5\sigma$  depths for point sources are given in column 5. Fluxes used in SED fitting and plotted in Figures 1 & 2 are given in column 6 (full arc) and column 7 (Earendel individually), along with 68% confidence uncertainties.

IMF	Stellar Mass Density
	$(M_{\odot} \text{ pc}^{-2})$
Chabrier	$8 \left[ \begin{smallmatrix} 17 \\ 0.7 \end{smallmatrix} \right]$
Salpeter	$15 \left[ \begin{smallmatrix} 30 \\ 1.0 \end{smallmatrix} \right]$

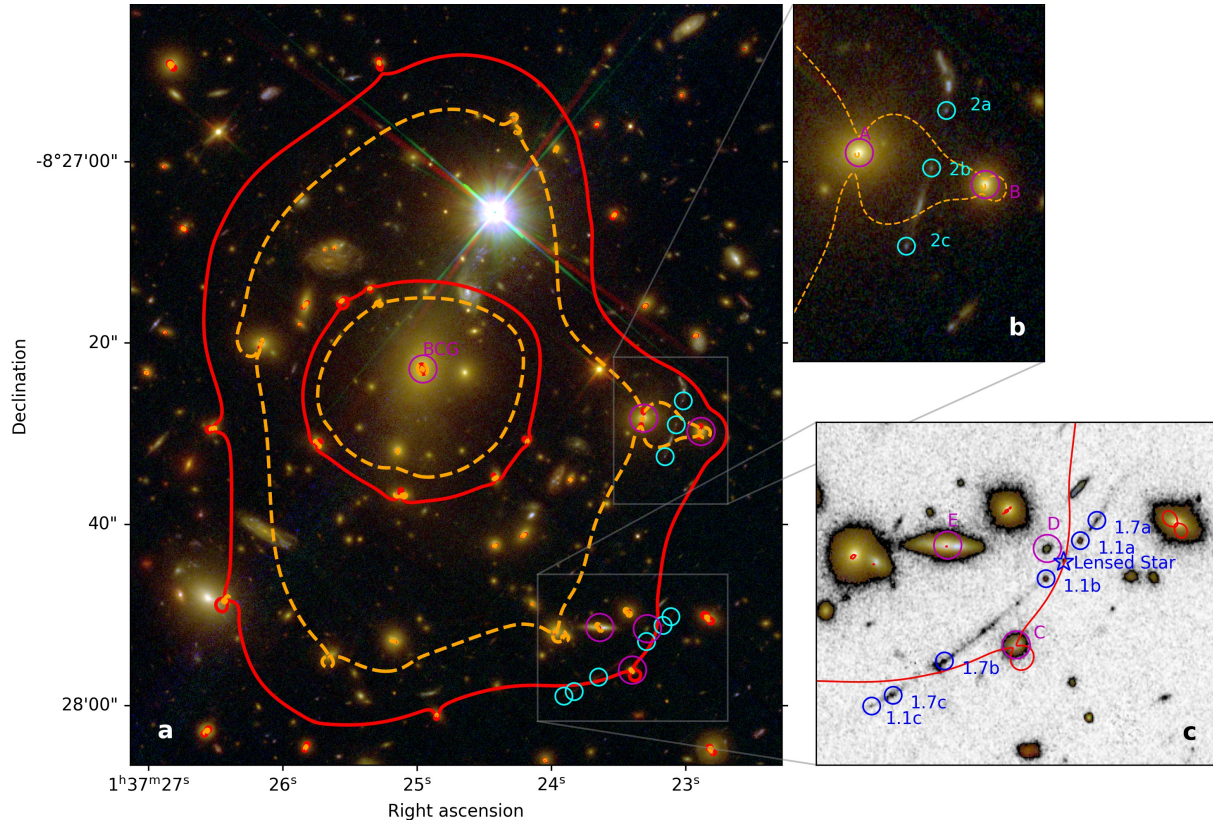
**Extended Data Table 2.** Stellar surface mass densities from two possible IMFs. These values include both ICL and the wings of cluster member galaxies. Most likely values are followed by 68% confidence ranges in brackets.



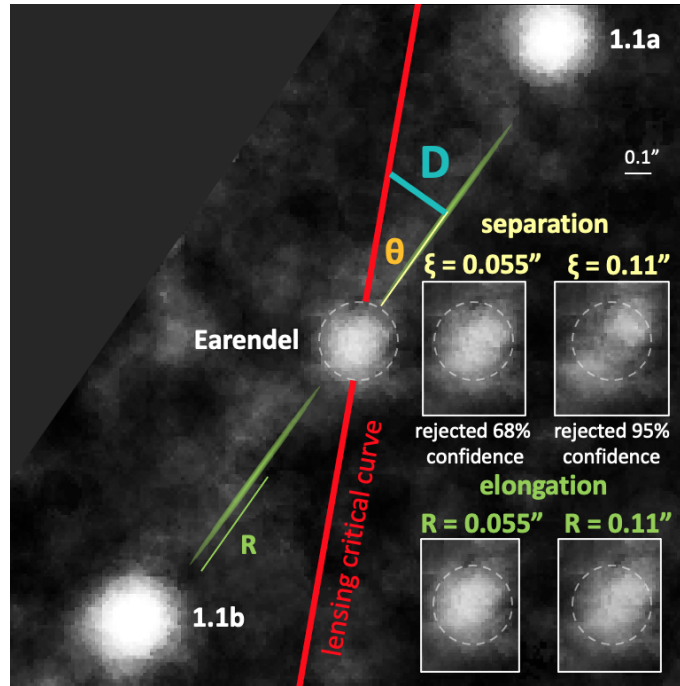
**Extended Data Figure 1. Photometry of the Sunrise Arc and Earendel a**, *HST* photometry with  $1\sigma$  error bars, SED fit, and redshift probability distribution for the Sunrise Arc using the photometric fitting code BAGPIPES. The arc shows a clear Lyman break feature, and has a photometric redshift  $z = 6.24 \pm 0.10$  (68% CL). **b**, *HST* photometry for the full arc (black), clumps 1.1a/b (green/blue), and Earendel (red), with associated  $1\sigma$  error bars. BPZ yields a photometric redshift of  $z_{\text{phot}} = 6.20 \pm 0.05$  (inset; 68% CL), similar to the BAGPIPES result. Clumps 1.1a/b have similar photometry, strengthening the conclusion that they are multiple images. Note both BPZ and BAGPIPES find significant likelihood only between  $5.95 < z < 6.55$  for the Sunrise Arc.



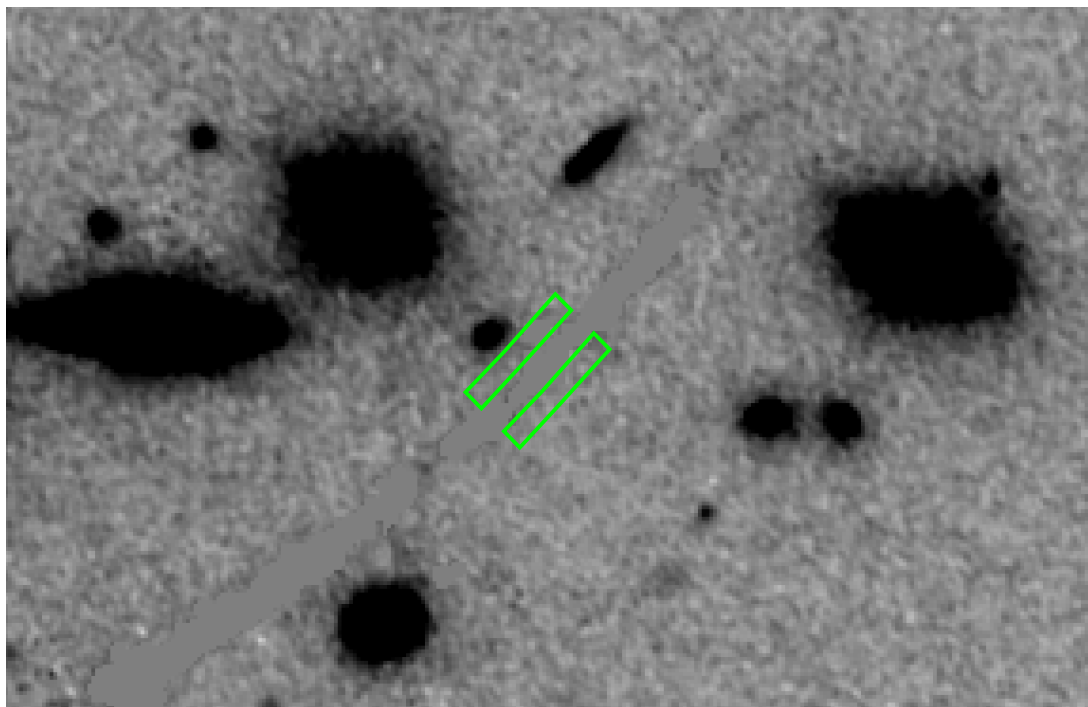
**Extended Data Figure 2. Lensed star variability across observations** Earendel has remained consistently bright across 3.5 years of *HST* imaging. Panels **a-d** show WFC3/IR images of the lensed star (circled in green) across four epochs. Panels **a** and **b** show epochs 1 and 2 respectively, taken as part of RELICS, and are a sum of the IR imaging in 4 filters F105W+F125W+F140W+F160W from each epoch (one orbit each). Panels **c** and **d** show follow-up F110W imaging taken in epochs 3 and 4 respectively (one orbit each, in a more efficient filter). Panel **e** shows a plot of the original RELICS photometry (blue) compared to the follow-up photometry (orange), each with  $1\sigma$  error bars. The blue band is the weighted average of the original RELICS IR fluxes ( $35 \pm 9$  nJy, 68% CL), while the orange band is the new F110W flux ( $49 \pm 4$  nJy, 68% CL).



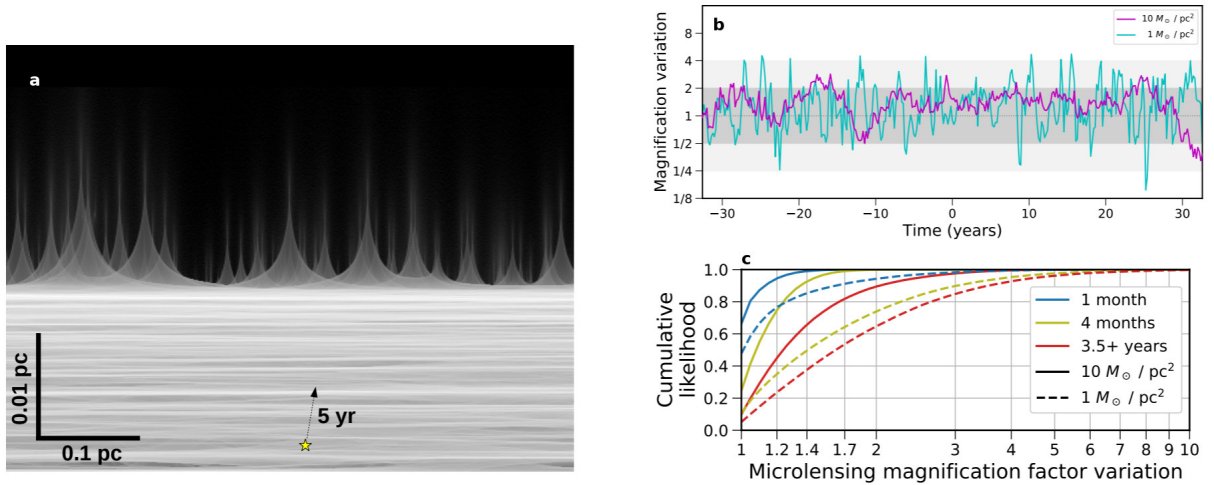
**Extended Data Figure 3. Strong lens modeling constraints for WHL0137–08 a**, *HST* composite image of WHL0137–08, a massive galaxy cluster at  $z = 0.566$  which lenses the Sunrise Arc. Multiple images of the two lensed galaxies used in the lens modeling are marked in cyan and labeled in zoomed insets. Cluster member galaxies circled in magenta are those freely optimized in both the LTM and Lenstool lens models. Critical curves are shown for the best-fit LTM model. The dashed orange curve is at  $z = 3.1$ , the same photometric redshift as multiple image system 2 (shown in **b**), while the solid red curve is at  $z = 6.2$ , the photometric redshift of the Sunrise Arc (system 1, shown in **c**). The lensed star Earendel lies directly between 1.1a and 1.1b. Note that 1.1c appears fainter than its counter-images 1.1a/b due to its lower magnification and all of these images being unresolved.



**Extended Data Figure 4. Size and separation upper limit measurements** Earendel's image is spatially unresolved. We manipulate this image, separating it in two or stretching it in place to put upper limits on its magnified radius  $R < 0.055''$  and distance  $2\xi < 0.11''$  between two unresolved images. These constraints allow us to calculate constraints on the intrinsic radius  $r$ , distance  $D$  to the critical curve, and magnification  $\mu$  for each lens model. Here we show a zoomed region of the arc around Earendel in a 10x super-sampled reconstruction of our HST WFC3/IR F110W image based on 8 drizzled exposures. The distances and radius labeled in the diagram are exaggerated for visibility.

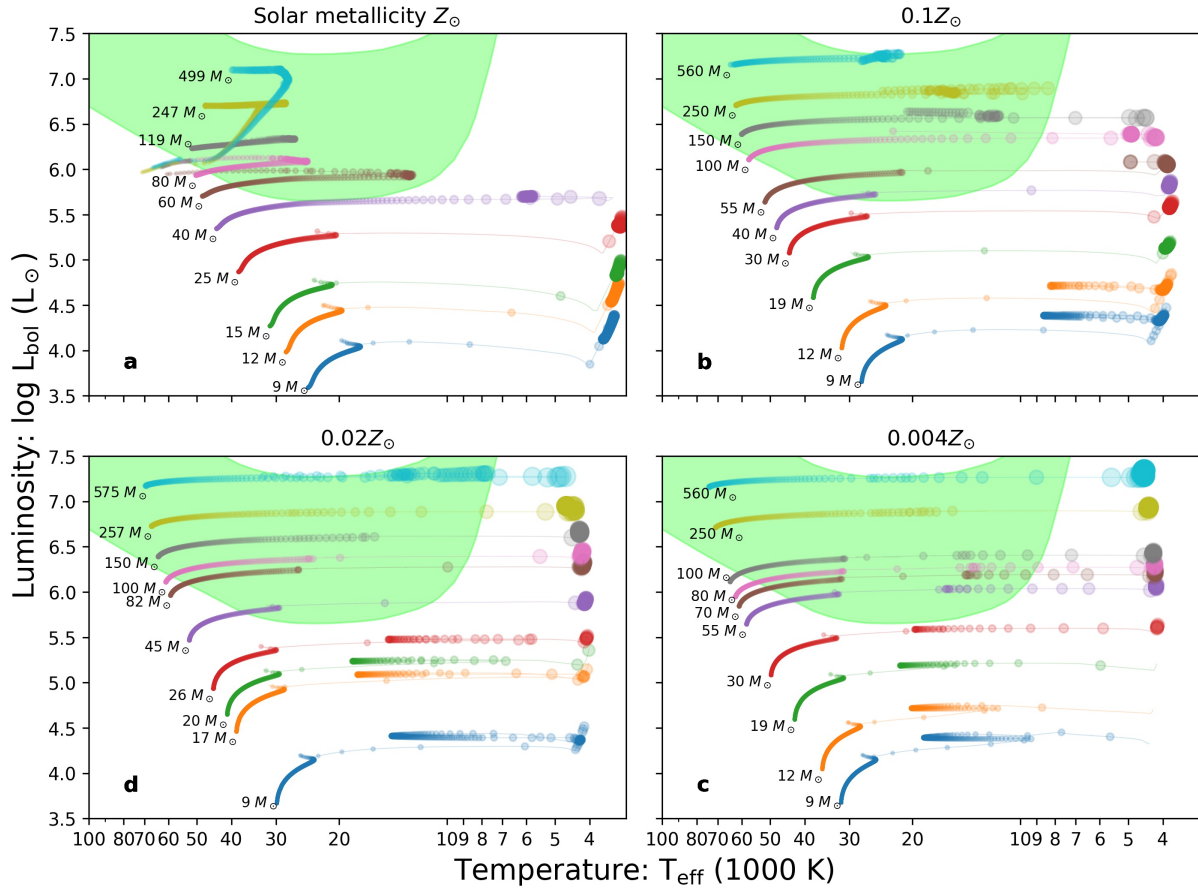


**Extended Data Figure 5. Diffuse cluster light measurements** Stellar surface mass density calculations are performed in the vicinity of the lensed star, within the green boxes shown. The arc and star are masked to avoid contamination, but nearby cluster galaxies are included. This figure shows the *HST* F110W band image, which is used to define the extent of the lensed arc.

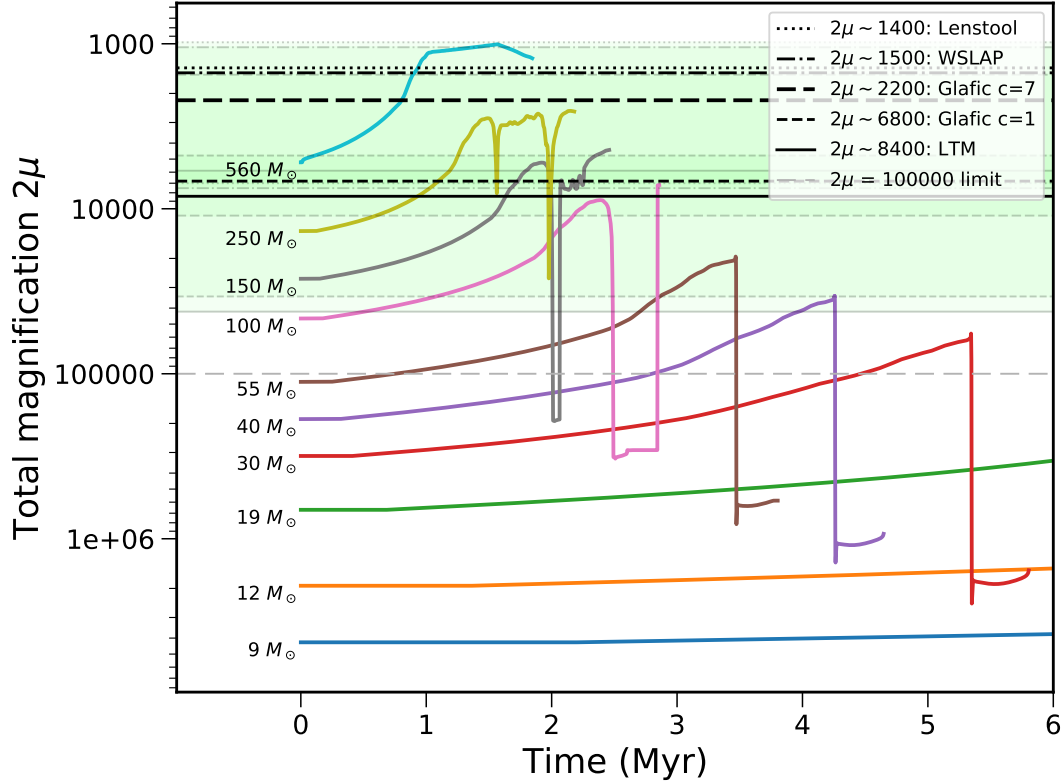


**Extended Data Figure 6. Flux variations expected from microlensing simulations** Microlensing is only expected to vary the total magnification by a factor of 2 – 3 over time, consistent with the observed steady flux over 3.5 years. Panel **a** shows the simulated microcaustic network arising from stars and stellar remnants within the lensing cluster. The cluster caustic is the extreme magnification horizontal region near the middle of the image, with individual cusps from microlenses still visible beyond the cluster caustic. We estimate Earendel will move relative to the microlens network at  $\sim 1000 \text{ km s}^{-1}$  in some unknown direction. Panel **b** shows predicted magnification fluctuations over time arising from this motion in the  $1 M_{\odot} \text{ pc}^{-2}$  case (blue) and the  $10 M_{\odot} \text{ pc}^{-2}$  case (purple), assuming that the relative motion is at an angle of  $45^{\circ}$ . Grey bands highlight a factor of 2 (dark) and a factor of 4 (light) change in magnification. Panel **c** shows the likelihood of magnification variations between two observations separated by different times, again for both the 1 and  $10 M_{\odot} \text{ pc}^{-2}$  cases. Note the *more is less* microlensing effect that reduces variability in the observed images when the density of microlenses increases.





**Extended Data Figure 7. H-R diagrams with stellar tracks at multiple metallicities** A star’s metallicity will impact its evolution, so to probe this effect we show here our luminosity constraints compared to stellar tracks from BoOST at metallicities of 1, 0.1, 0.02, and 0.004 $Z_{\odot}$  (panels **a**, **b**, **c**, **d** respectively). The 0.1 $Z_{\odot}$  case is also shown in Figure 3, and these plots are similar, including the green region allowed by our analysis. While the tracks do exhibit some notable differences, the resulting mass estimates do not change significantly given the current large uncertainties.



**Extended Data Figure 8. Stellar evolution tracks versus time** Here we show the total magnification required to lens stars to Earendel’s apparent magnitude as a function of time on stellar evolution tracks (BoOST  $0.1Z_{\odot}$ , as plotted in the HR diagram Figure 3). This required magnification changes over the lifetime of each star as it varies in luminosity or temperature, changing the flux observed in the F110W filter. We find that stars at  $\sim 100M_{\odot}$  and above spend the most time ( $\sim 2$  Myr) in the green region reproducing Earendel’s observed flux, given our magnification estimates. But considering that lower mass stars are more numerous, we conclude that masses of roughly  $\sim 50 - 100M_{\odot}$  are most likely if Earendel is a single star.